Journal of Dynamic Behavior of Materials (2019) 5:266–295
https://doi.org/10.1007/s40870-019-00210-1

S.I. : TEMPERATURE DEPENDENCE OF MATERIAL BEHAVIOUR AT HIGH STRAIN-RATE

Dynamic Response of Advanced Materials Impacted by Particle Beams: The MultiMat Experiment

M. Pasquali[1] · A. Bertarelli[1] · C. Accettura[1,2] · E. Berthome[1] · L. Bianchi[1] · P. Bolz[3] · F. Carra[1] · C. Fichera[4] · M. I. Frankl[1] · T. Furness[5] · G. Gobbi[1] · P. Grosclaude[1] · J. Guardia-Valenzuela[1,6] · M. Guinchard[1] · M. D. Jedrychowsky[1,7] · F. J. Harden[1] · A. Lechner[1] · P. Mollicone[8] · P. D. Pastuszak[1] · M. Portelli[8] · S. Redaelli[1] · E. Rigutto[1] · O. Sacristan de Frutos[1] · P. Simon[3]

Received: 2 May 2019 / Accepted: 13 July 2019 / Published online: 19 July 2019

Abstract
The introduction at CERN of new extremely energetic particle accelerators, such as the high-luminosity large hadron collider (HL-LHC) or the proposed future circular collider (FCC), will increase the energy stored in the circulating particle beams by almost a factor of two (from 360 to 680 MJ) and of more than 20 (up to 8500 MJ), respectively. In this scenario, it is paramount to assess the dynamic thermomechanical response of materials presently used, or being developed for future use, in beam intercepting devices (such as collimators, targets, dumps, absorbers, spoilers, windows, etc.) exposed to potentially destructive events caused by the impact of energetic particle beams. For this reason, a new HiRadMat experiment, named "MultiMat", was carried out in October 2017, with the goal of assessing the behaviour of samples exposed to high-intensity, high-energy proton pulses, made of a broad range of materials relevant for collimators and beam intercepting devices, thin-film coatings and advanced equipment. This paper describes the experiment and its main results, collected online thanks to an extensive acquisition system and after the irradiation by non-destructive examination, as well as the numerical simulations performed to benchmark experimental data and extend materials constitutive models.

Keywords Dynamic material behaviour · Thermomechanical stresses · Carbon-based and copper composites · Molybdenum and tungsten alloys · Particle beam impacts · Quasi-instantaneous heat deposition

Introduction

The LHC [1] is the largest and most energetic particle accelerator in the world, with two counter rotating proton beams with an energy of 360 MJ each, which are brought into head-on collisions in four detectors.

In the coming years, the energy stored in each of the two beams will be almost doubled to 680 MJ with the high luminosity LHC (HL-LHC) upgrade [2], aimed at substantially increasing the accelerator performances. This trend is set to become even more compelling in the proposed future circular collider (FCC) [3], which is expected to increase the energy stored in the circulating hadron beams (FCC-hh) by almost a factor of 20 with respect to the LHC, reaching up to 8500 MJ. Furthermore, these energies are concentrated in a very small volume, since the typical cross-section of a particle beam at top energy is in the order of a few tenths of millimetres.

✉ M. Pasquali
michele.pasquali@cern.ch

1 CERN, Esplanade des Particules 1, 1211 Geneva 23, Switzerland

2 Politecnico di Milano, Piazza Leonardo da Vinci 32, 20133 Milan, Italy

3 GSI Helmholtzzentrum, Planckstrasse 1, 64291 Darmstadt, Germany

4 ITER, Route de Vinon-sur-Verdon, 13067 St. Paul-Lez-Durance, France

5 University of Huddersfield, Queensgate, Huddersfield HD1 3DH, UK

6 University of Zaragoza, Calle de Pedro Cerbuna 12, 50018 Saragossa, Spain

7 AGH University of Science and Technology, WFilS, Al. Mickiewicza 30, 30-059 Kraków, Poland

8 University of Malta, Msida 2080, Malta

It is therefore paramount to assess the thermomechanical response of materials presently used, or being developed for future use, in those components that are inherently subjected to potentially destructive events caused by the impact of particle beams as targets, dumps, absorbers or collimators (see Fig. 1), usually called beam intercepting devices (BID) [4].

In this article, we will deal with studies and experiments related to the collimators for the HL-LHC; however, the general concepts and main findings can be extended to any BID for particle accelerators and, more broadly, to any device submitted to rapid and intense heating.

The HL-LHC collimation system is composed of a large number of collimators placed in various locations of the accelerator ring. These devices are designed to intercept and absorb the intense particle losses unavoidably induced in accelerator normal operation and to shield other components from the catastrophic consequences of beam orbit errors, in particular related to an abnormal injection or extraction of the particle beam [5]. The most meaningful accidental design scenarios are the beam injection error (BIE), which assumes that a full train injected into the HL-LHC hits the absorbers of a primary or secondary collimator jaw, and the Asynchronous Beam Dump (ABD), in which a full HL-LHC bunch at 7 TeV hits a tertiary collimator jaw [6, 7].

The MultiMat (also named HRMT36) experiment was designed to gather experimental data upon which building or validating reliable constitutive models for materials subjected to the impact of beam pulses of intensity comparable or higher than those expected in HL-LHC accidental scenarios. Successfully performed in autumn 2017 at CERN HiRadMat facility [8], its scope was, in particular, to derive or validate little known material properties, such as mechanical response at high strain rates, dynamic strength, internal damping, effects of porosity, anisotropic wave propagation and dynamic behaviour of coatings.

The experiment profited of the experience of previous tests carried out at the CERN HiRadMat facility. In HRMT09 [9], carried out in 2012, a full LHC collimator, with a tungsten alloy as absorbing material, was tested to observe the effects of accidental direct beam impacts, benchmark simulations and derive acceptable limits for this absorbing material [10]. In HRMT14 [11], also performed in 2012, specimens of simple geometry, extensively instrumented, were impacted with particle beams to benchmark the numerical results obtained with different FE codes (namely, ANSYS [12], Autodyn [13] and LS-Dyna [14]). Results confirmed the precision of the numerical results when the material models match reasonably well the extreme conditions induced by particle beam impacts [15, 16]. In 2015, the HRMT23 (also named "Jaws") [17] experiment validated the design of the jaws made of novel metal-diamond and ceramic-graphite composites designed for HL-LHC collimators, achieving energy densities exceeding those expected for HL-LHC. In 2017, the HRMT21 experiment saw the testing of a low-impedance secondary collimator featuring a faceted rotatable jaw [18], made of a dispersion-strengthened copper, with 20 collimating surfaces to be successively used in case of beam damage.

One of the main elements of novelty of MultiMat with respect to previous experiments was the adoption of slender rods as targets for the beam impacts. This was meant to allow reaching values of deposited energy per cross-section exceeding those achieved in impacts on full collimators jaws [5, 9, 17, 18] or on targets featuring larger cross-sections [11], in spite of the lower pulse intensity. In fact, the total amount of energy deposited over a cross-section is, as it will be shown, a key driver of the material response.

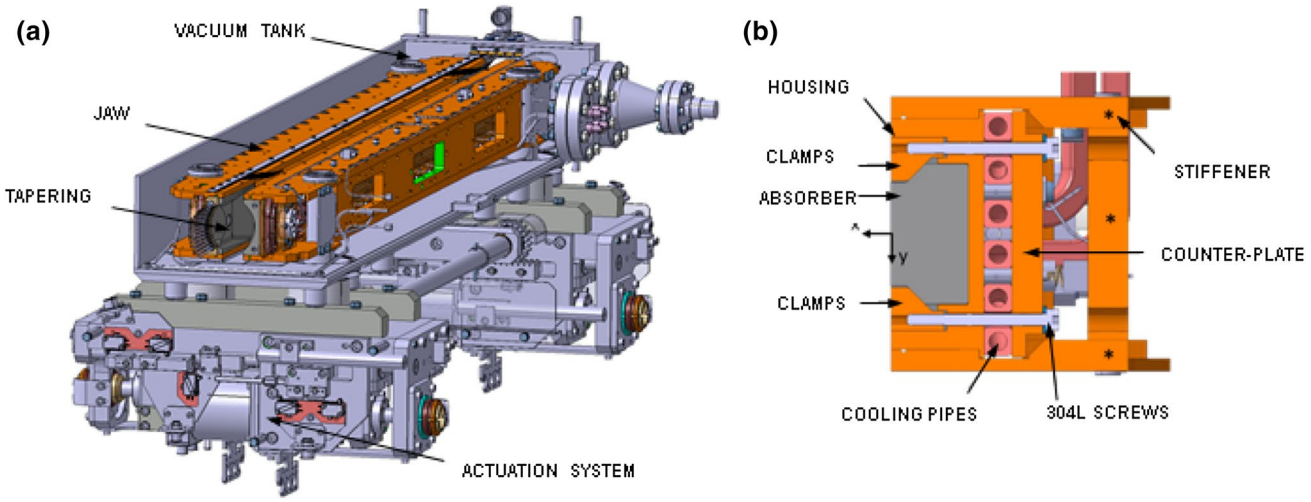

Fig. 1 Cutaway drawing of a HL-LHC secondary collimator (**a**) and transverse cross-section of the collimator jaw (**b**)

A total of 81 specimens, made of 18 different materials, were tested in a comprehensive experimental setup. Six different material groups were studied, namely, pure carbon materials, metal carbide–graphite composites, additively-manufactured titanium alloy, copper–diamond composites (CuCD), silicon carbide (SiC) as well as molybdenum, tungsten and tantalum heavy alloys. Samples were submitted to different types of impacts, with the intensity of the beam pulses progressively increased and reaching energy densities up to 10^4 J cm^{-3} deposited in less than 10 µs.

The experimental campaign, which allowed gathering a very large amount of data, was complemented by a series of in-depth numerical analyses. Such simulations relied on finite element codes reproducing the experimental response of each specimen impacted by proton pulses, in order to confirm or infirm the validity of the adopted constitutive models. For each impact, energy deposition maps were obtained from FLUKA [19], a Monte Carlo code simulating interaction and transport of atomic and subatomic particles in matter. The thermal energy maps produced by energy deposition codes were then imported in the numerical model, constituting the input for the dynamic simulations. Given the foreseen absence of changes of phase in the impacted samples in the experimental scenarios, numerical analyses were performed with the implicit code ANSYS. Thermal transient simulations were run first: structural simulations then made use of the derived temperature field to evaluate the dynamic mechanical response of the samples.

Dynamic Response of Materials Subject to Quasi-Instantaneous Heating

When subatomic particles or swift ions interact with matter, they tend to transfer part of their energy to the medium they traverse; this energy loss is ultimately turned into heat and leads to an increase of the temperature in the impacted target [20]. Depending on the amount and distribution of the deposited energy and the time-scale of the phenomenon, i.e. the density of deposited power, different effects may result. If the deposited power density is sufficiently high, dynamic responses will be induced, principally because the thermal expansion of the impacted material is initially prevented by its inertia, giving rise to isochoric (constant-volume) heating [21]. This can be the case, for instance, of accidental beam impacts on collimators [10], as opposed to nominal operating conditions, which typically lead to slow transient or quasi-static responses. From a thermomechanical standpoint, the problem can be reduced to the study of a body subjected to a non-uniform, quasi-instantaneous heat generation lasting the time of the beam interaction τ: this deposition time is of the order of few microseconds, thus generally much shorter than both the period T of the waves generated by the impact and the heat diffusion time t_d [22]. The quasi-instantaneous, beam-induced thermal load generates dynamic stresses propagating through the material at the velocity of sound, akin to a structure mechanically struck by another massive body.

The nature and intensity of the dynamic responses depend on several parameters, mainly the total amount of energy deposited, its distribution, the duration of the impact, the thermo-physical and mechanical properties of the impacted material, and the form and dimensions of the object interacting with the beam.

Figure 2 provides an overview of the different types of dynamic response that might be induced in a structure as a function of the density of the deposited power and the duration of the interaction. It can be inferred that the dynamic response eventually depends on the specific energy deposited on the material.

In spite of the large influence of material properties and differences in designs, some approximate general figures can be extrapolated and used as a guideline to predict the type of dynamic response, to a first approximation, regardless of the affected material and of the boundary conditions. If the density of the deposited energy is below 100 J cm^{-3}, the dynamic response will probably remain within the *elastic dynamic regime*, meaning that the induced vibrations and stress waves will not exceed the elastic limit of the material and that the structure will return to its initial undeformed state at the end of the process. Between roughly 100 J cm^{-3} and 10 kJ cm^{-3}, we may expect that, particularly for metals, the stress waves will locally exceed their elastic limit, inducing permanent plastic deformations that cannot be recovered once the dynamic response has died out (*plastic dynamic regime*). Above 10 kJ cm^{-3}, the stress waves may be strong enough to generate major changes of density and extensive damage to the material, such as extended cracks, fragmentation or explosion. If the impacted material is metal, phase transitions with the formation of liquid, gas, or plasma usually may occur: this is usually referred to as the *shock wave regime*. Furthermore, if a significant reduction in density has occurred in the impacted material while particle bunches are still interacting with the body, the beam will penetrate further and further, given that fewer atoms are available to interact with the incoming particles: this effect is sometimes called *hydrodynamic tunnelling* [23]. It usually arises, within the shock wave regime, when the duration of the impact is sufficiently long to allow changes of phase to develop (several 100 ns or more).

The study of such dynamic phenomena, particularly when dealing with the shock-wave regime or hydrodynamic tunnelling, is usually accomplished resorting to sophisticated numerical analyses. Unfortunately, the material models required to perform such simulations at extreme conditions are hardly available in scientific literature. For these reasons,

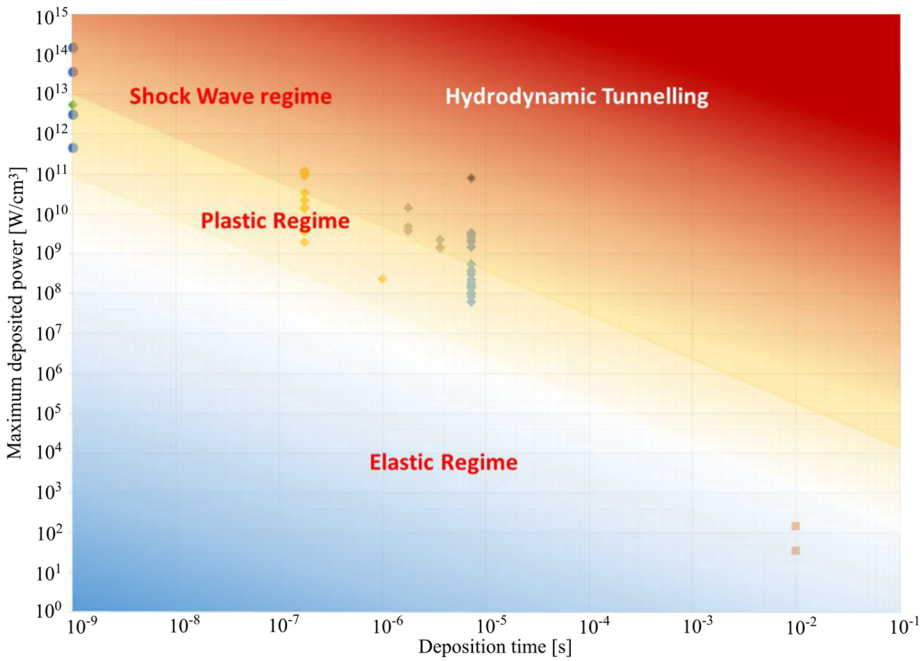

Fig. 2 Plot of maximum deposited power density versus duration of deposition, showing the different dynamic responses that can be induced in matter by interaction with particle beams. Points represent cases of beam impacts (real or simulated) of previous studies [20]

dedicated tests in experimental facilities using intense and energetic particle pulses are often required to derive or validate the constitutive models of relevant materials.

In this respect, it is worth remarking that experiments resorting to particle beam impacts allow to study regions of the materials equations of state (EOS) diagram (pressure, density, internal energy) that are hardly accessible with conventional dynamic experiments as the Hopkinson bar test, the flyer plate impact test, the Taylor test, etc. Limitations of mechanical tests are usually encountered in the study of the material expansion phase, especially in case of changes of phase implying vapour and plasma. In fact, to reach such states during the isentropic release phase, extremely high shock-induced pressures are needed. This is observable in Fig. 3a for the case of a beam impact [22]. The material is initially at the point O of the diagram and is then subjected to a sudden internal energy rise ΔE, which corresponds to an increase in temperature and pressure up to the point $1'$. Given the small deposition time τ, the material does not experience a change in volume, because this is prevented by its mass inertia, therefore density remains constant. In this phase, the material is under compression and may undergo a change of phase, if the thermal energy is high enough. At the end of the pulse, the material relaxation begins; point 2

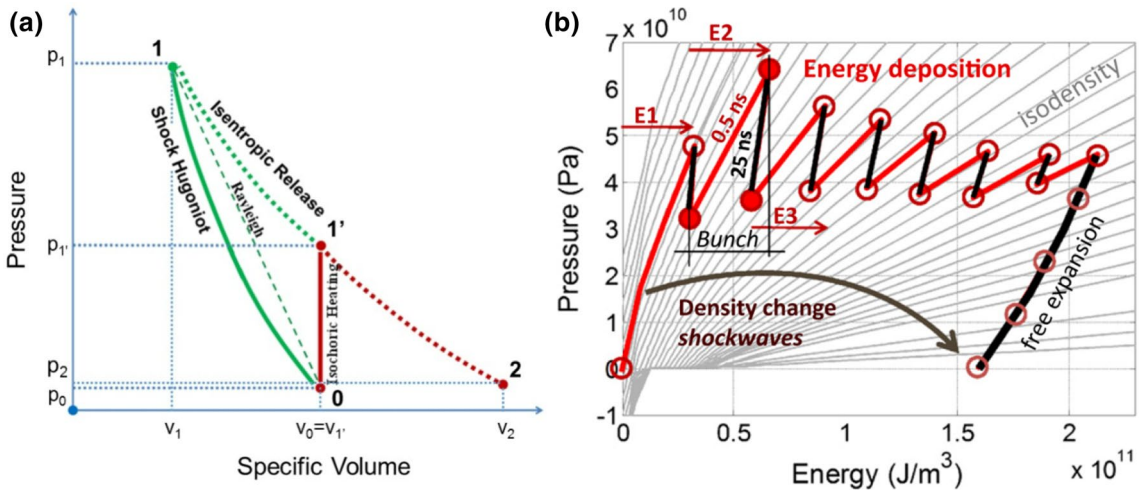

Fig. 3 Comparison between a mechanical shock (0–1–2) and an isochoric heating event (0–1′–2) (**a**) [22]. Equation of state of copper: during the energy deposition phase, the symbols identify the material conditions after each bunch arrival and after 25 ns from its arrival (**b**) [24]

is a generic position on the release path, where the material pressure is p_2.

In the case of a mechanical impact, in order to achieve the same conditions 1′, the material must first experience a much higher shock pressure and density (position 1). In the release phase, the material expands, crossing the position 1′, before reaching the condition 2. It is therefore much easier to reach conditions of high temperature and internal energy in an isochoric heating test with respect to a conventional mechanical impact experiment. This is also confirmed by Fig. 3b, where the effects of an 8 bunch-pulse on a copper target are shown [24]. It is possible to observe that each bunch impacting the sample after the first one causes a much more significant increase in energy density, and thus in temperature, than in pressure, which in turn remains almost constant or even decreases.

The MultiMat experiment achieved on tested materials peak energy densities as high as 10^4 J cm^{-3}, with deposition times shorter than 10 μs: according to Fig. 2, this may translate into dynamic responses laying in the upper limit of the plastic regime, possibly encompassing also failure phenomena. It is very important to notice, that, given the slender geometry chosen for the MultiMat samples, significant effects can be driven, on top of those induced by the peak energy density, by the total average energy deposited on the specimens cross-sections, as it will be shown in the following.

Theoretical Considerations

As shown in previous studies [21], the behaviour of MultiMat samples, which can be treated as long cylinders, can be analytically studied as the sum of a quasi-static contribution, which is obtained treating the heated body as axially and transversally constrained, and a dynamic contribution, which is superimposed to restore the exact boundary and initial conditions. To simplify the analytical approach, we assume isotropic, linear elastic materials, with no internal damping and with properties independent of temperature.

Let us consider a cylindrical rod of length L and radius R, made of an isotropic, homogeneous material with Young's modulus E, density ρ and thermal expansion coefficient α, whose radius is much smaller than its length, so that radial dynamic effects can be neglected, submitted to a rapid temperature rise induced by an internal non-uniform heat generation during a time τ. Let the energy deposition be constant along the rod axis, with a transversely offset Gaussian distribution over the rod cross-section (Fig. 4a).

Assuming that no heat diffusion occurs during the impact because the characteristic thermal diffusion time t_d is much longer than the impact duration τ, the rod sees a rapid temperature rise linearly proportional to the deposited energy. On the same ground, the system can be considered adiabatic during a typical time of at most several milliseconds. This allows estimating the temperature profile over the rod cross-section, as shown in Fig. 4b.

Once the temperature distribution is known, it is possible to obtain the quasi-static stresses in cylindrical coordinates adapting a method developed by Goodier [25]. It is first assumed that radial expansion can freely occur while longitudinal expansion is blocked, thus resulting into a zero longitudinal strain condition. The quasi-static stress distribution for such a condition on any rod cross-section at the end of the energy deposition $t=\tau$ is shown in Fig. 5. These stresses tend to wane as heat diffuses and temperature distribution becomes uniform (T_f), with the exception of the longitudinal stress, which converges to a uniform value $\sigma_{\mathrm{Ref}} = E\alpha T_f$ resulting from the compression induced in a rod with fixed ends by the uniform temperature T_f.

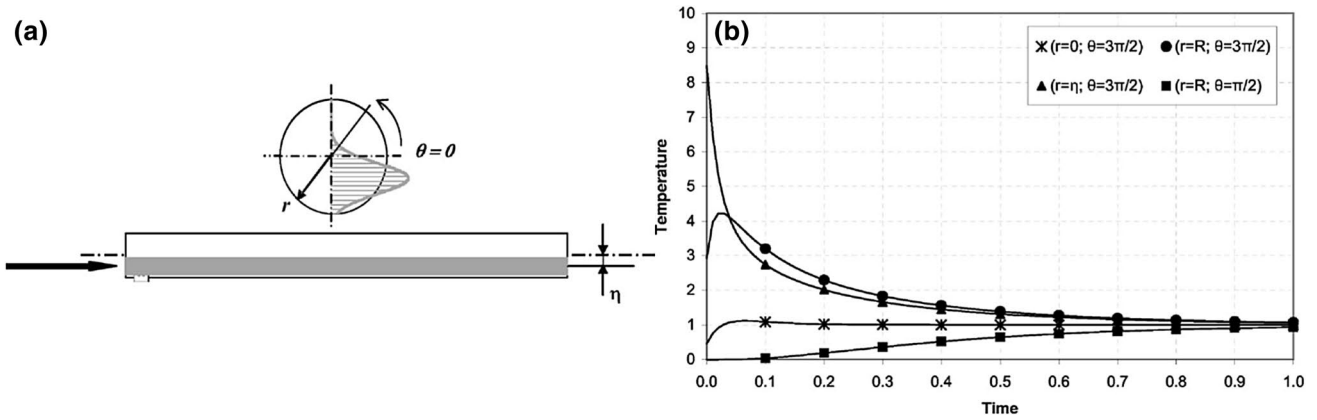

Fig. 4 Energy distribution on a cylindrical rod due to a particle beam impact centred at $r=\eta$ and $\theta=3\pi/2$ (**a**), and the resulting non-dimensional temperature profile Θ over the time $\bar{t}=(t-\tau)/t_d$ on the rod cross-section, scaled with respect to the final uniform temperature T_f in adiabatic conditions expected on the sample (**b**) [21]

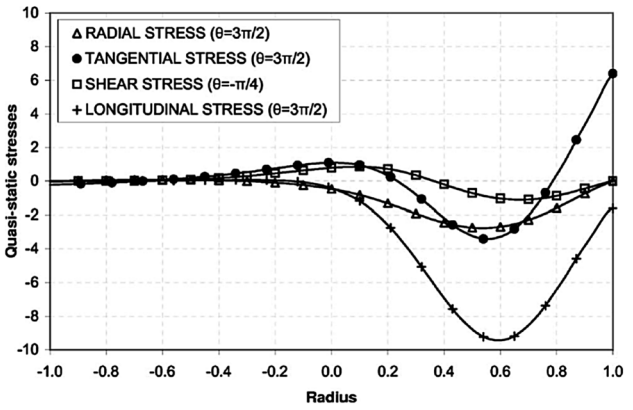

Fig. 5 Radial, tangential shear and longitudinal quasi-static in-plane stresses as function of the non-dimensional radius of the cylindrical rod [21]

In reality, the rod is axially free at its extremities, where longitudinal stresses become zero: to restore such condition, we apply at both ends of the rod the opposite of the axial force $F(t)$ and bending moment $M(t)$ resulting from the distribution on the cross-section of longitudinal stresses at zero total strain. As for temperature, these loads grow up linearly from zero to the maximum value at the end of the energy deposition τ; from this time on, $F(t)$ remains constant, since it can be shown that it is proportional to the total deposited energy, while $M(t)$ decreases as the temperature distribution tends to become uniform through thermal diffusion.

The application at both ends of the axial force $F(t)$ gives birth to dynamic stresses propagating along the rod axis as two elastic stress waves moving from the extremities of the rod, which superpose to the quasi-static stresses shown in Fig. 5, relaxing the initial compressive state. Figure 6a shows the evolution over time of the longitudinal dynamic stress. The two stress waves then superimpose at the centre and get reflected at the other end. The values are scaled with respect to σ_{Ref}: the longitudinal dynamic stress oscillates between zero and twice the reference stress value, depending on the way the two waves interact.

It is interesting to note that this relation holds until the energy deposition time τ is smaller than half of the longitudinal wave propagation period $\Gamma_z = 2L/c_z$, where $c_z = \sqrt{E/\rho}$ is the speed of sound along the length of the rod. If the energy deposition lasts longer than this, the heat-induced build-up of the longitudinal compressive state will be slower than the stress relaxation phenomenon occurring through wave propagation and the maximum longitudinal dynamic stress will never be reached, as can be observed in Fig. 7.

Since we have assumed that the heat distribution is radially offset, the resulting moment M(t) will additionally induce lateral oscillations whose associated stress field superimposes to that due to axial wave propagation.

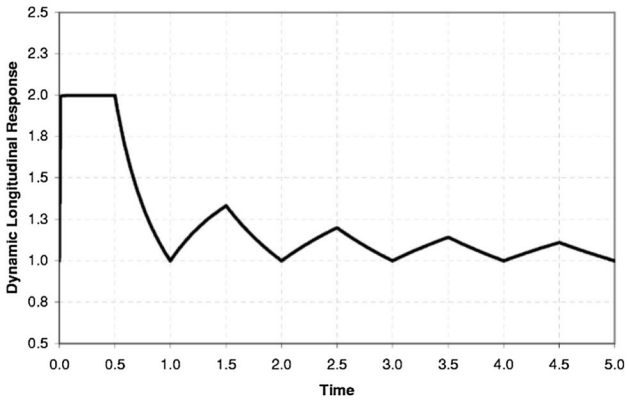

Fig. 7 The dynamic axial response scaled to the reference stress σ_{Ref} as a function of the ratio between the energy deposition duration τ and the longitudinal wave period Γ_z [21]

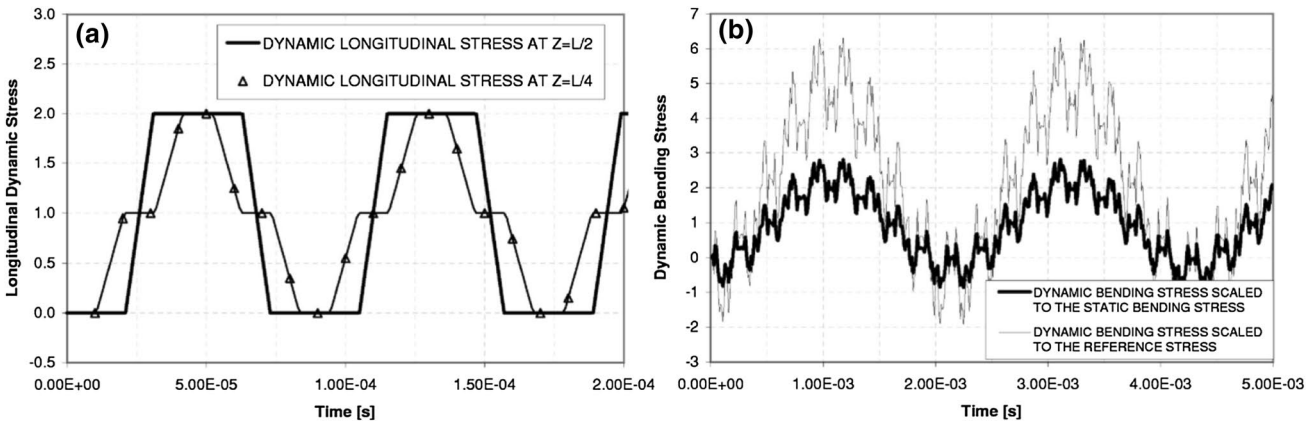

Fig. 6 Dynamic longitudinal stress scaled to the reference longitudinal stress σ_{Ref} as a function of time at different locations along the rod (**a**) and the dynamic bending stress at half of the length of the sample scaled with respect to the reference and to the static bending stress (**b**) [21]

Figure 6b shows that the dynamic bending stress can be almost three times larger than its static counterpart $\sigma_{fs} = M(\tau) \times J^{-1} \times R^{-1}$, J being the moment of inertia of the cylinder's cross-section, and more than six times larger than the reference longitudinal stress σ_{Ref}. The theoretical investigations presented in this section were numerically benchmarked in [22].

In the above analysis, it has been assumed that the dynamic contribution to stresses in the radial and tangential directions can be neglected, since the radius is very small compared to the rod length. Yet, it must be noted that this assumption is not always acceptable: in fact, one can argue that, if the heating process is sufficiently short, the rod is also initially radially constrained, i.e. $u(R) = 0$, where $u(r)$ is the radial displacement; in this hypothesis, the quasi-static stress components in the cross-section will modify accordingly, leading to non-zero radial stresses on the outer surface. Since the rod is free to expand in the radial direction, a relaxation cylindrical wave will depart from the outer surface and travel towards the axis with a radial period $\Gamma_r = \sqrt{E/\left[\left(1-\nu^2\right)\rho\right]}$, superimposing to the wave coming from the opposite direction, hence giving rise to alternate compressive and tensile stress contributions, akin to longitudinal waves described previously. The full development of the dynamic contribution in transverse direction depends on the ratio between the radial period and the energy deposition duration: in fact if the energy deposition time τ is larger than half of the radial waves propagation period Γ_r, the stress relaxation will propagate while energy is still being deposited. In this case, the dynamic contribution to the radial response can be small, with the total radial response converging quickly to its mere quasi-static component.

On the other hand, if $\tau < \Gamma_r/2$, the dynamic contribution to the radial response has enough time to reach its maximum, which is again two times σ_{Ref}, in both radial and tangential directions.

These phenomena are observable in Fig. 8: the plot in (a) shows the simulated mechanical tangential strains measured on the outer surface of a cylindrical rod whose geometrical and material parameters have been chosen to have $\tau = 4\Gamma_r$. As expected, the component of the response due to radial waves propagation is very small. On the contrary such contribution is shown to be dominant in Fig. 8b, where the condition $\tau = \Gamma_r/4$ is met.

In the considerations made so far, the energy deposition was assumed to be constant along the rod length. In case of a non-constant energy distribution, it is possible to define $\bar{U}_{\max}$ as the maximum value along the axis of the average energy density deposited over a cross-section of the rod:

$$\bar{U}_{\max} = \frac{1}{\pi R^2} \iint_{00}^{R2\pi} Urdrd\theta \Big|_{max} \tag{1}$$

Having assumed that no heat diffusion occurs during the heating period, the temperature $\bar{T}_{\max}$ at the end of the thermal shock at the most loaded cross-section can be simply calculated as $\bar{T}_{\max} = \bar{U}_{\max} / \rho c_p$. In the hypothesis made of isochoric heat deposition, the reference stress at most loaded cross-section thus amounts to $\sigma_{\mathrm{RefMax}} = E\alpha\bar{T}_{\max}$ both in the longitudinal and radial direction, as free expansion is prevented by inertia.

In the case of a constant energy distribution, $\bar{T}_{\max} = T_f$ and $\sigma_{\mathrm{RefMax}} = \sigma_{Ref}$: this means that every cross-section of the cylinder exerts the same dilatation-induced force on adjacent sections. As a result, the axial expansion starts at the rod's free edges and travels towards its centre in the shape of a step-like signal of constant amplitude, as already discussed.

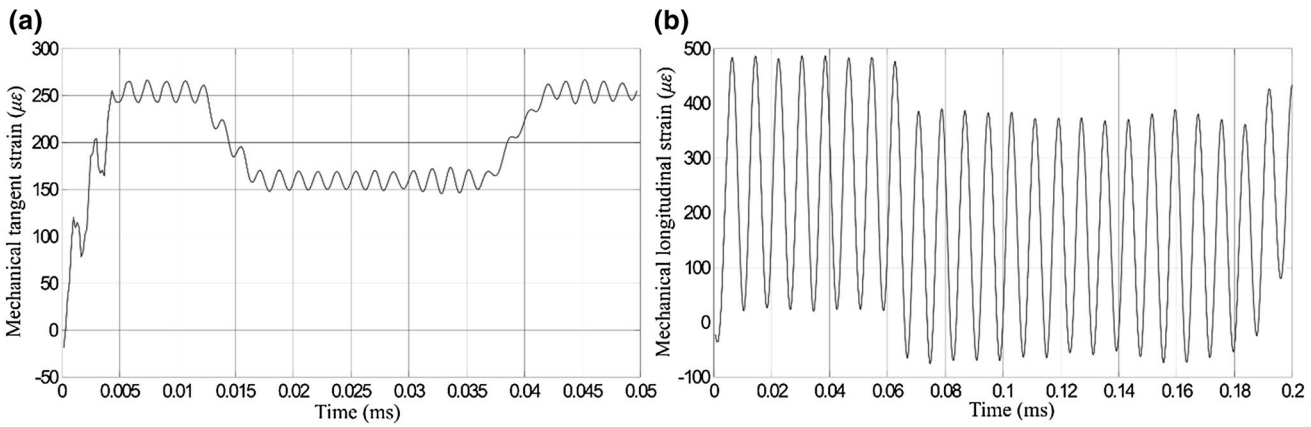

Fig. 8 The simulated mechanical tangential strains acquired on the outer surface of a cylindrical rod whose geometrical and material parameters were chosen to have $\tau = 4\Gamma_r$ (**a**) and $\tau = \Gamma_r/4$ (**b**), leading, respectively, to a minor and a dominant contribution of radial waves propagation to the tangential response of the rod

This is because each cross-section, experiencing the same compression state, contributes equally to the dilatational motion occurring longitudinally. Finally, if $\tau < \Gamma_z/2, \Gamma_r/2$ the rod exhibits longitudinal and radial dynamic components of its response equal to $2\sigma_{Ref}$.

If a non-constant energy distribution is considered, then $\bar{T}_{\max} > T_f$ and $\bar{\sigma}_{ref} > \sigma_{Ref}$. In this case, the various cross-sections of the cylinder do not experience the same rise in temperature. As a consequence, in the hypothesis of isochoric heating, the forces due to dilatation which are mutually exchanged by two adjacent sections along the rod axis are not balanced, leading to motion onset not only at the rod free faces but also within the cylinder. This results into compression waves of different amplitudes travelling and superimposing along the rod, which will be eventually reflected at the free faces as tensile waves of shape generally different from the step-like waves observed for constant energy distributions.

These considerations can be observed in Fig. 9 which shows the case of a cylindrical graphitic rod impacted by two beam pulses of identical total deposited energy and featuring, respectively, a constant $U^c(r,\theta,z) = U^c(r,\theta)$ and a parabolic $U^p(r,\theta,z)$ energy density distribution along the rod axis, the latter having its maximum at the centre of the rod and going to zero at its extremities. In particular the two distributions are such that $\bar{U}^p_{\max} = 3/2\bar{U}^c_{\max}$.

Figure 9a, b show the temperature field occurring over the sample at $t = \tau$ for the two cases: since U^p exhibits a higher energy density peak $U^p_{max} > U^c_{max}$, then a higher maximum temperature $T^p_{max} > T^c_{max}$ is also reached locally. Moreover, while with a constant energy distribution the longitudinal expansion at the end of the energy deposition is confined to the regions close to the free faces (c), almost the entire rod is already set in motion in the case of a parabolic energy density distribution (d). The different shape of the energy density distribution affects also the quasi-static longitudinal state of stress estimated along the rod axis.

On this regard, it is interesting to notice that the longitudinal stress distributions in Fig. 9e, f (normalized with respect to σ_{Ref}) mimic the respective energy density distributions, with the ratio between the peak (absolute) values in the two cases coinciding almost with the ratio $\bar{U}^p_{\max}/\bar{U}^c_{\max}$ (the difference being mainly due to specific heat c_p of graphite increasing with temperature).

Finally, longitudinal stresses are acquired on the outer surface of the cylindrical rod at mid axis, where the quasi-static component is expected to be close to zero (~ − 2 MPa). The mentioned step-like longitudinal wave (g) travels along the rod in presence of a constant energy density distribution, while a much smoother longitudinal wave occurs when considering a parabolic energy density distribution (h). Also in this case, the ratio between the amplitudes of the two stress waves $\sigma^c_{z_d}$ and $\sigma^p_{z_d}$ is close to that existing between the maximum average energy densities, as $\sigma^p_{z_d}/\sigma^c_{z_d} = 2\bar{\sigma}^p_{ref}/2\bar{\sigma}^c_{ref} \cong \bar{U}^p_{\max}/\bar{U}^c_{\max}$. The same relationship holds for the dynamic component of the radial response, e.g. for the tangent stresses acquired at the same point, as shown in Fig. 9i, j.

It is interesting to notice that the longitudinal motion of Fig. 9d occurring along the entire rod already during the energy deposition phase, can lead, by momentum conservation, to axial oscillations of the centre of gravity of the rod when a longitudinally asymmetric non-constant energy density distribution is considered. Figure 10 shows the axial displacement of the center of gravity of the graphitic cylindrical rod induced by the constant energy density distribution and by the parabolic distribution considered so far having its maximum displaced at $z = L/4$. As a consequence, axial oscillations of the centre of gravity, which stayed confined to the range of numerical errors for a constant distribution, rise.

The results discussed above, together with the considerations made so far, show that the dynamics of the impacted rod is driven by the maximum average energy density $\bar{U}_{\max}$ deposited over its cross-sections. This fact helps understanding the additional benefit of the MultiMat experiment compared to previous tests. The choice of impacting slender rods of small transverse cross-section instead of typical BID parts subject to beam interaction (as collimator's blocks), in fact, allowed reaching larger values of $\bar{U}_{\max}$ adopting beam pulses of maximum intensity similar to that achieved in previous experimental campaigns.

Consequently, during MultiMat it was possible to explore the behaviour of the tested materials at higher stress and strains levels, as it will be shown in the following.

Numerical Simulations

One of the goals of the MultiMat experiment was to benchmark the numerical models of the tested materials at levels of stress and strain higher than those achieved in previous tests. Material models were mostly built on the basis of static measurements, made at CERN and elsewhere, as well as from datasheets provided by suppliers.

Tested materials included also advanced composites, in some cases created and developed at CERN in collaboration with international partners, for which literature is scarce; the available data allowed building only constitutive models which are sometime independent of temperature and strain rate. Additionally, these constitutive models are becoming more and more inaccurate with the increase in deposited energy, when strong nonlinearities are expected.

Numerical analyses consisted of a chain of simulations including the energy deposition code FLUKA [19] and the implicit finite element (FE) code ANSYS [12]. FLUKA provides the deposited energy density in GeV cm^{-3} calculated

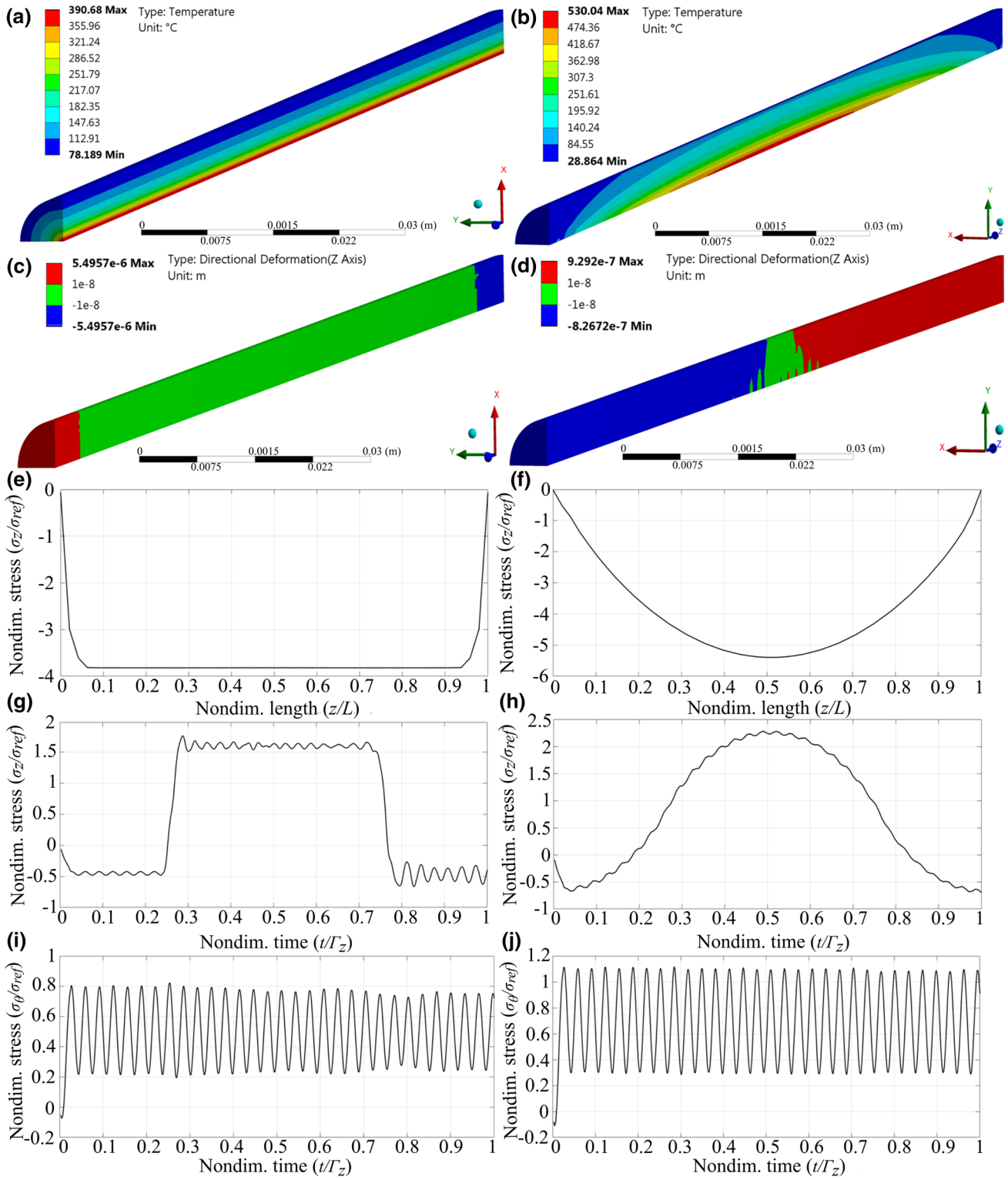

Fig. 9 The simulated thermomechanical response of a graphitic cylindrical rod subject to a constant energy density distribution along its axis (left column) and to a parabolic energy density distribution featuring the same total deposited energy (right column). Temperatures (**a**, **b**), longitudinal displacements (**c**, **d**) and longitudinal stresses (normalized to σ_{Ref}) on the axis (**e**, **f**) occurring at the end of energy deposition are shown. The longitudinal (**g**, **h**) and the tangent (**i**, **j**) non-dimensional stresses versus time (normalized to the axial wave period Γ_z) on the outer surface of the rod at $z = L/2$ are also displayed

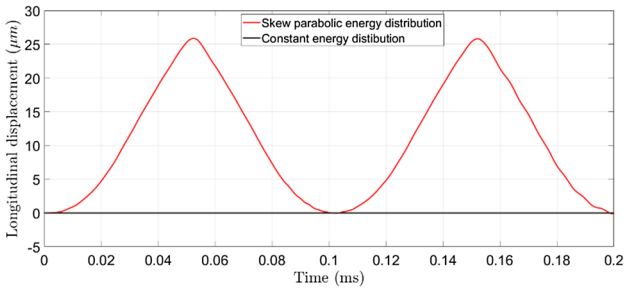

Fig. 10 The longitudinal displacements of the centre of gravity of a cylindrical rod subject to a beam pulse with constant and longitudinally asymmetric parabolic energy density distributions

at each element of the mesh and normalized to one proton. This needs, then, to be scaled according to the total particle intensity of the beam. When a beam impacts a sample, the interaction generates secondary particles, called particle shower that may in turn be absorbed by the material. Therefore, the energy deposition is a material–dependent feature. High-density and high-atomic number materials have high energy-stopping power and thus high energy density will be induced during the impact.

The energy deposition maps produced by FLUKA were then imported in the finite element codes as an input for the thermomechanical simulations. Given the type of the models adopted (elastic or elastoplastic) and the expected absence of changes of phase, we decided to perform numerical analyses relying on the implicit solver of ANSYS. This required less time steps with respect to explicit codes, making possible to simulate longer scenarios, as for the analysis of flexural oscillations of the impacted samples.

Thermal transient simulations were run first: structural analyses then made use of the temperature fields at each sub-step to evaluate in time the dynamic mechanical response of the samples.

Experiment Description

This section gives a brief overview of the facilities used to carry out particle beam impacts at CERN as well as a description of MultiMat design, acquisition system and protocol. An introduction to the materials that are the object of the present manuscript is also provided.

The HiRadMat Facility

Experimental testing of materials under beam impacts can be performed in facilities such as high radiation to materials (HiRadMat) at CERN. The facility operates as one of CERN Super Proton Synchrotron (SPS) [26] users: experiments in HiRadMat are run in single-pulse mode, with a beam request submitted each time via the SPS control system. In the case at hand of a proton beam, a maximum stored energy of 3.4 MJ at 440 GeV and a bunched pulse length of 7.95 μs can be achieved [8].

Different impact scenarios, with variable energy densities, can be explored by changing the pulse intensity (i.e. its total number of particles) and the beam size at the target. The density of the impacting beam, in the plane orthogonal to the propagation direction, approximately follows a Gaussian distribution. The parameter σ is its standard deviation and defines the beam transverse size. The HiRadMat allowable σ—range is 0.25–2 mm [8]. To minimize the radiation dose absorbed by personnel during the installation and exchange of experiments, a simple platform hosting the test-bench and allowing a rapid connection is used, as shown in Fig. 11.

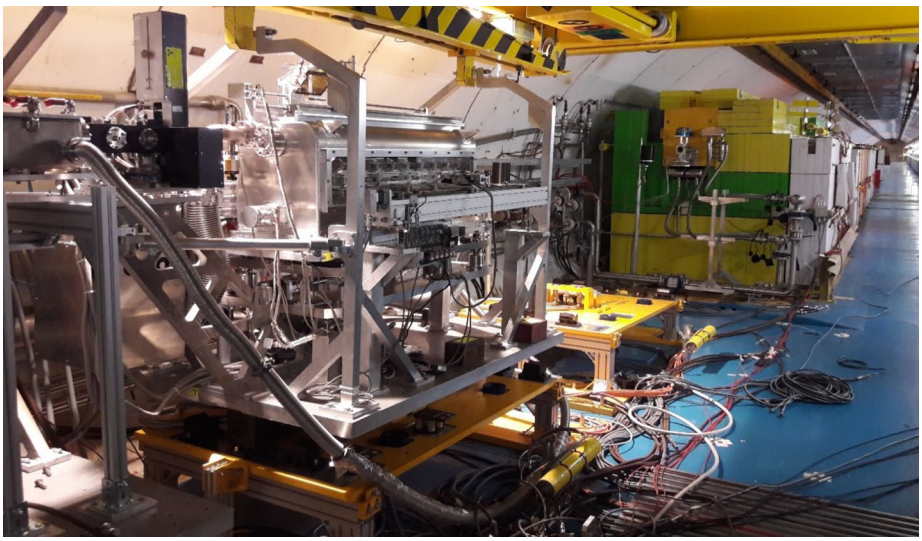

Fig. 11 The MultiMat setup being installed in the HiRadMat experimental area

The platform can be positioned using fixed mechanical references with a precision of 0.1 mm. Services like water-cooling, electrical power and signal cables are delivered via plug-in connectors.

Overview of MultiMat Design

The MultiMat test-bench featured a leak-tight aluminium vessel hosting 16 target stations (15 material lines plus a parking position), each 1-m long, mounted on a rotatable barrel allowing to bring each station into impact position (Fig. 12).

Aluminium was preferred to other materials (e.g., stainless steel) to achieve smaller activation levels. To rotate the barrel, a Geneva mechanism was designed to attain ± 180° rotation angles in steps of 22.5°, each one corresponding to the position of a line of specimens. Each target station could be finely aligned with respect to the beam by a precise actuation system: ± 15 mm of vertical and lateral actuation could be implemented resorting to a system of stepper motors, gearbox and end-stop switches (Fig. 13).

Each target station hosted a variable number of material specimens, in the form of slender bars supported, at the two extremities, by graphite restraints, with pressed contact granted by springs, as shown in Fig. 14. The samples tested in the experiment had cross sections ranging from 8×8 mm^2 to 12×11.5 mm^2 and lengths of 120 mm or 247 mm. These geometries allowed disentangling relevant phenomena, namely, power deposition, axial wave propagation, flexural oscillations and heat diffusion.

A forced flow of argon was provided by a closed circuit to ensure an inert atmosphere, limiting materials oxidation while decreasing the cooling time of the specimens after impact, to ensure a faster pulse repetition rate. A pressure difference (Δp) with room conditions of about ~ 0.1 atm was applied to prevent activated material particles to exit the tank. The aluminium vessel featured two viewports, one on the top and the other on the tank

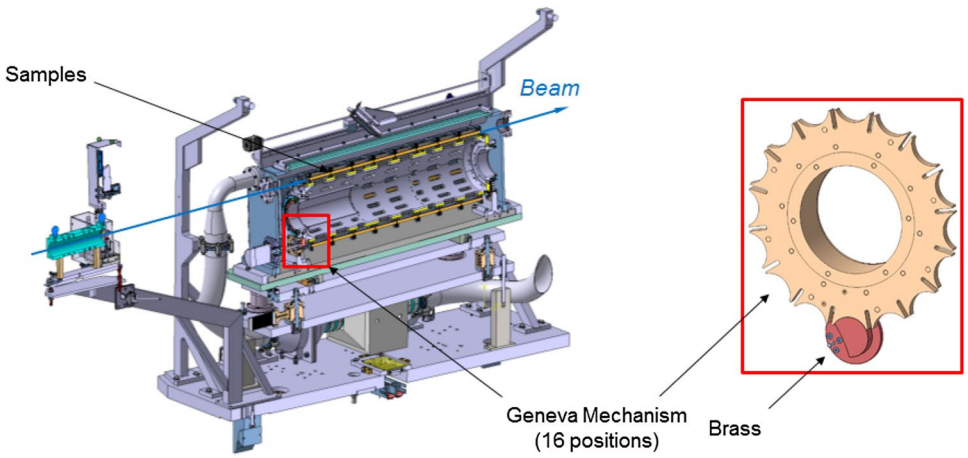

Fig. 12 Schematic representation of the MultiMat setup, with a cross-section view showing a zoom of the Geneva mechanism adopted to rotate the barrel hosting the different lines of specimens

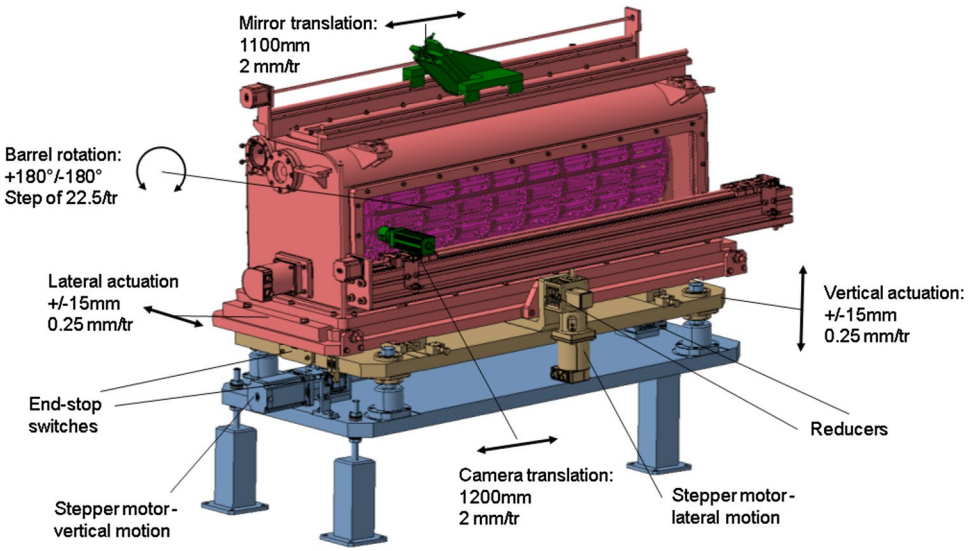

Fig. 13 The actuation system of the MultiMat experiment

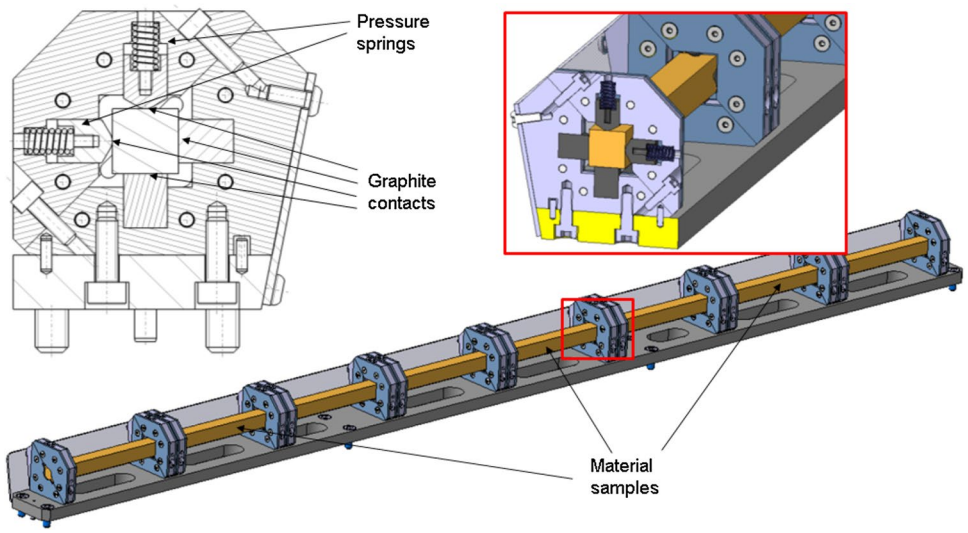

Fig. 14 Schematic representation of a MultiMat target line with its sample supports

side, to allow online measurements and offline observations. A radiation-hardened camera was mounted on the side of the vessel to allow observations of the impacted specimens immediately after each pulse, scanning the overall line thanks to a stepper motor-driven lateral slider (Fig. 15a). The top viewport was instead designed to allow the use of a Laser Doppler Vibrometer (LDV) system to acquire in real time the beam-induced vibrations of the samples (Fig. 15b). Each of the viewports featured an optically-transparent, temperature and radiation resistant window, designed to withstand possible impacts of fragments ejected by the irradiated specimens. Finally, the vessel was equipped with windows made of beryllium and carbon fibre-reinforced carbon (CFC) at the beam entry and exit ports to minimize the interaction with the particle beam, ensuring at the same time leak tightness and structural resistance.

Acquisition System

Experimental data were acquired on-line resorting to both extensive embedded instrumentation and remote acquisition devices. In particular, material samples were instrumented with 335 electrical resistive strain gauges and 112 platinum resistance thermometers (Pt-100) in total (Fig. 16a), the former being mounted to record impact-induced stress waves propagating in the specimens, while the latter were meant to measure temperature variations caused by the energy deposition. In order to limit the thermal impedance between the specimens and the thermometer, Pt-100 sensors were bonded to the sample surface using a thermally conductive epoxy-based glue, which was however expected to debond at temperatures above 150 °C [27].

For strain measures, in order to optimize the accuracy of the acquisition against the amount of data to be stored, a sampling frequency of 4 MHz was kept for the first 23 ms (plus additional 3 ms before the pulse arrival at the sample location), then decreasing to 100 Hz for the rest of the

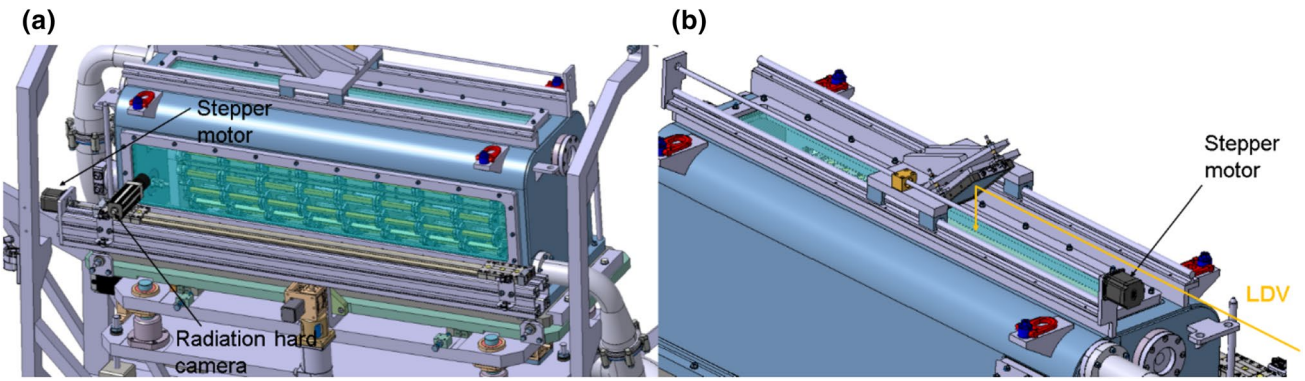

Fig. 15 The radiation-hard camera (**a**) and the LDV (**b**) installed on the MultiMat setup

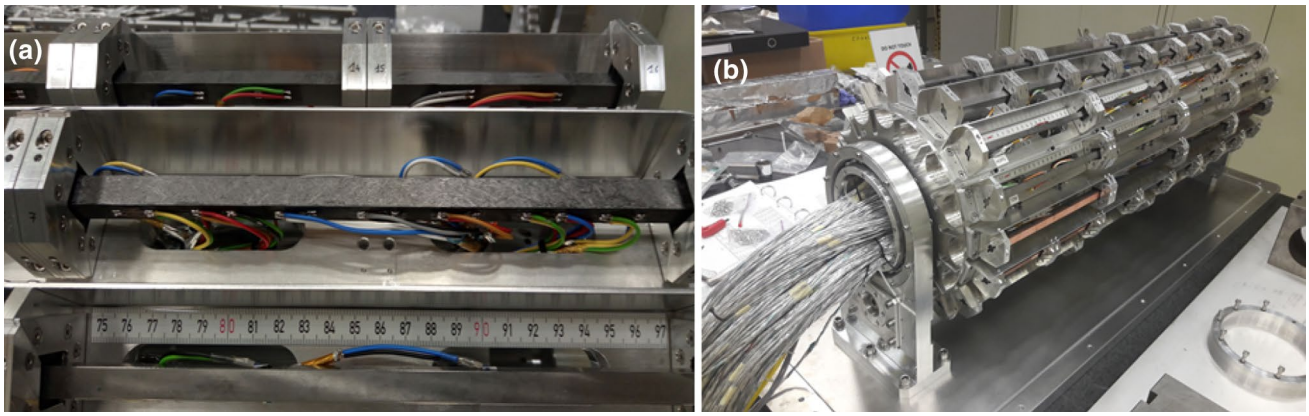

Fig. 16 The fourth sample of the CFC AC150 K line of MultiMat instrumented with temperature probes and strain gauges (**a**) and the barrel hosting all the sensors connections (**b**)

acquisition, which lasted 30 s. This allowed achieving the accuracy needed to well resolve both the fastest dynamic phenomena occurring in the samples after the impact (such as transversal and longitudinal wave propagation) and slower phenomena, as flexural oscillations of the specimens and heat diffusion. The 100 Hz sampling rate was adopted also for the temperature measures. A cut-off frequency of 900 kHz was chosen for strain measures to enhance their signal-to-noise ratio, with an 11-points Savitzky-Golay windowing applied to reduce signal spectral leakage [28]. It is worth noticing that in the first few microseconds after the impact the strain gauge signals are affected by a strong electromagnetic disturbance induced by the passage of the (electrically charged) proton beam. This effect rapidly decays so that the net strain measurements become clearly visible after 10–30 µs, depending on the intensity of the pulse.

In addition to the embedded sensors, an LDV, installed in a shielded remote bunker to protect it from the effect of radiation, measured the velocity of the top surface of the impacted specimens, as shown in Fig. 15b. A system of precisely aligned mirrors was put in place to reflect the LDV laser beam onto the specimens and send it back to the vibrometer. Also in this case, a cut-off frequency of 900 kHz was used for the acquired signal, together with a 31-points Savitzky-Golay time-windowing. A radiation-hard camera was additionally installed on the experiment setup to visually inspect each line after being impacted. During the impacts, the camera was positioned upstream with respect to the beam to protect it from particle shower. After the impact, the barrel was rotated to bring the impacted line behind the lateral viewport for inspection (Fig. 15a). A digital acquisition system (DAQ), featuring NI PXIe-6124 modules, was set up to gather data coming from the various measuring devices; its characteristics are reported in Table 1.

During the test, the DAQ allowed to synchronize all measuring equipment to a trigger associated to beam pulse arrival. Due to limitations regarding the number of available cables at the HiRadMat facility, a radiation-hard multiplexing hardware (1:8 out/in ratio), developed during HRMT23, was also installed on the test-bench. Since underground HiRadMat facilities (Fig. 2) were not accessible during the test run, the multiplexer control was transferred to the surface control room. Given the high radiation level expected during the experiment, only radiation-hardened equipment could be installed in the setup. All embedded components (strain gauges, thermal probes, adhesives, cables and connectors) had a radiation resistance to doses higher than those expected during the experiment [29].

Finally, both a Beam TV (BTV) and a Beam Pick-up Gauge (BPKG) monitor, shown in Fig. 17, were directly embarked on the experiment test-bench to check the beam size and position, respectively, complementing the beam-monitoring equipment already present at the HiRadMat testing area.

Table 1 Principal characteristics of the digital acquisition system

	Measure type	Acquisition range	Quantity	Sensor type	Sampling rate
Electrical devices	Strain	100–5000 µm m^{-1}	335	Strain gauges	4 MHz/100 Hz
	Temperature	− 55 to 155 °C	112	PT100	100 Hz
Optical devices	Surface velocity	< 0.1 to 24 m s^{-1}	1	LDV	4 MHz
	Visual inspection	–	1	Rad-hard camera	40 fps

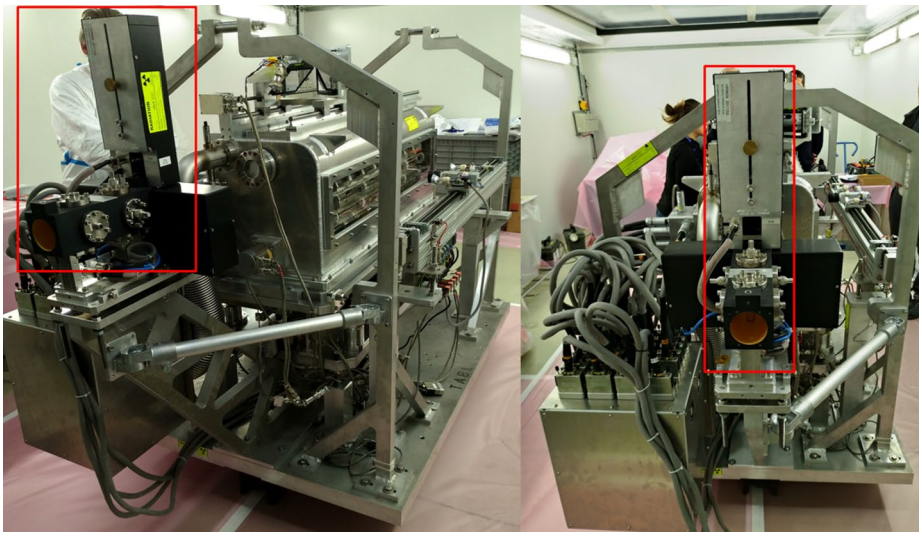

Fig. 17 The BTV and BPKG embarked on the MultiMat test-bench to monitor the beam position and size

Overview of Tested Materials

As mentioned, 18 different materials were tested during the MultiMat experiment in the form of slender rods with cross sections dimensions ranging from 7×8 mm^2 to 12×11.5 mm^2 and lengths of 120 mm or 247 mm (see Table 2).

These materials were chosen as they are of interest to respond to the increasingly challenging requirements posed by BID to be installed in future high-energy accelerators such as HL-LHC or FCC. For instance, the material currently employed for the absorbers of primary and secondary collimator jaws for the LHC (AC150 K, a two-dimensional Carbon–Carbon composite) [30] is predicted not to satisfy the full set of requirements imposed by the severe working conditions expected in the HL-LHC from 2026. In particular, the limited electrical conductivity of CFC may induce electro-magnetic instabilities in the particle beam.

In this context, a family of graphite-matrix composites, reinforced with molybdenum carbides (Molybdenum Carbide–Graphite, MoGr) was co-developed by CERN and an Italian SME, Brevetti Bizz [31], with the goal of increasing the electrical conductivity of the materials for the primary and secondary collimator jaws, while maintaining

Table 2 The materials tested in MultiMat

#	Material	Description	Density [g cm^{-3}]	Coating
1	IT180	Tungsten–nickel–copper alloy	18.0	
2	Ta10 W	Tantalum–tungsten alloy	16.9	
3	Ta2.5 W	Tantalum–tungsten alloy	16.7	
4	TZM	Titanium–zirconium–molybdenum alloy	10.0	
5	CuCD-G1	Copper–diamond composite	5.40	
6	CuCD-G2	Copper–diamond composite	5.40	
7	SiC	Silicon–carbide	3.21	
8	MG6403Fc	Molybdenum–graphite composite	2.54	5 µm TiN
9	NNK265-266	Molybdenum–graphite composite	2.52	
10	MG6530Aa	Molybdenum–graphite composite	2.50	2 µm Cu
11	MG6541Fc	Molybdenum–graphite composite	2.49	8 µm Mo
12	TPG	Thermal pyrolytic graphite	2.26	
13	TG1100	Titanium–graphite composite	2.19	
14	R4550	Isotropic graphite	1.90	2 µm Cu
15	CFC AC150 K	Carbon–carbon composite	1.88	8 µm Mo
16	Ti6Al4 V	Additively-manufactured titanium alloy	1.62	
17	CFOAM	Carbon foam	0.40	
18	Al6082-T651	Aluminium alloy	2.70	

the beam impact robustness close to that of CFC [32, 33]. MoGr is the baseline material for primary and secondary collimators for the HL-LHC.

MoGr is produced by spark plasma sintering (SPS), starting from powders of graphite, molybdenum and, in some grades, carbon fibres and titanium. SPS, a variation of hot pressing also known as field-assisted sintering technique (FAST) or pulsed electric current sintering (PECS), is a powder metallurgy technology that combines uniaxial mechanical pressure and the application of electrical current to the system. The sintered material heats up by Joule effect. The temperatures reached during the sintering, in excess of 2600 °C, allow melting the molybdenum carbide formed during the process, exploiting the advantages of liquid phase sintering. Molten carbides induce catalytic graphitization by the dissolution of individual carbon atoms, eventually connecting them to form high quality solid graphite.

This continuous dynamic dissolution–precipitation process dissolves the most disordered and hence most reactive carbon structures—such as amorphous regions or unconnected edges of basal planes—and precipitates ordered graphite that grows and bridges the initial graphite crystallites [33].

The intrinsic morphology of the graphite matrix and the manufacturing process lead to a transversely isotropic material: the in-plane and perpendicular directions are defined as those parallel and perpendicular to the graphite basal planes, as shown in Fig. 18.

Several grades of MoGr were developed in order to optimize key thermophysical, mechanical and UHV properties: those tested in MultiMat include MG6403Fc, MG6530Aa, MG6541Fc produced by Brevetti Bizz. MG6530Aa is an early MoGr grade which was tested in HRMT23 in 2015; MG6403Fc and MG6541Fc are two grades doped with titanium to reduce material anisotropy, thanks to the different carbide lattice. Two samples made of a grade produced by a Spanish company, Nanoker (NNK265-266), were also tested, even if this grade was still at an early phase of development at the time of test.

A titanium carbide-graphite grade (TG-1100) was also tested to explore less dense carbide-graphite compounds, potentially alternative to MoGr.

On top of MoGr and CFC, other commercially available carbonaceous materials are used or considered for BID, with some of them tested in MultiMat: these include isotropic polycrystalline graphite (grade R4550) [34], thermal pyrolytic graphite (TPG) [35] and graphitic foams (C-Foam) [36].

TPG is manufactured from thermal decomposition of hydrocarbon gas at high temperature. It is produced by the dissociation of hydrocarbon gases in a chemical vapour deposition process. This leads to an epitaxial growth of graphene layers with only little defects concentration. The high alignment of the graphene layers enhances the thermal and electrical conductivities of the material along the basal planes. Due to the nature of strongly aligned graphite structure, the material is highly anisotropic, having very different properties in the through-plane direction, compared to the in-plane. In particular, one of the main drawbacks is its very low strength in the through-plane direction.

Carbon foams are very low-density materials with high porosity in which most of the macropores (cells) are interconnected by graphite ligaments, leading to an open cell structure. They have novel features due to their cell structure, such as large geometric surface area, associated with the fundamental properties characteristic for carbon materials, i.e., low density, high thermal stability, hydrophobic surface nature, high thermal and electrical conductivities, etc.

To further increase the electrical conductivity of the surface exposed to the beam, a thin film of electrically conductive metals or ceramics can be coated onto MoGr, as well as to other dense graphitic materials. Tested solutions include molybdenum, copper and titanium nitride coatings applied on MoGr, CFC and polycrystalline graphite.

Copper–diamond (CuCD) is a proposed alternative to the tungsten heavy alloys currently adopted in LHC tertiary collimators. This material is, in fact, much more robust to proton beam impacts. CuCD was developed with the goal of combining the main advantages of its two

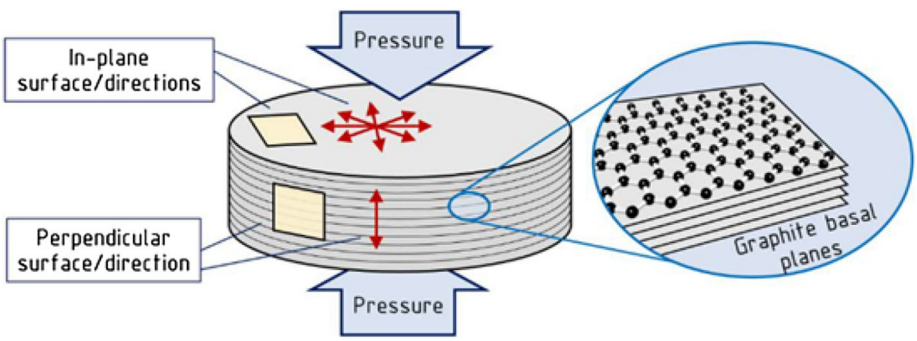

Fig. 18 Preferred orientation of graphite basal planes with respect to the uniaxial pressure applied during the sintering process. Naming convention for the in-plane and through-plane/perpendicular material directions

constituents: copper and diamond. Its thermal properties exceed those of pure copper, while diamonds strongly reduce the thermal expansion coefficient and the density of the composite with respect to the pure metal [37]. Two different grades were tested in MultiMat (CuCD-G1 and CuCD-G2).

Additional materials which were investigated include heavy alloys, mostly based on molybdenum (titanium–zirconium–molybdenum alloy, TZM), tantalum (tantalum–tungsten alloy, Ta10 W and Ta2.5 W) and tungsten (tungsten–nickel–copper alloy, Inermet180®, denoted as IT180) [38, 39]. IT180 is presently used in LHC tertiary collimators. Silicon carbide (SiC) [40], which is expected to possess high thermomechanical robustness appealing also for other applications outside particle accelerators (aerospace, nuclear plants, braking elements) and additively-manufactured Ti6Al4V samples, produced at CERN with an internal lattice structure of various cell sizes (2.5 mm and 5 mm) associated to an external thin skin (0.5 mm), are possible candidates for application in those areas of BID where high structural resistance combined to low beam cleaning performance is required.

In addition to the above-mentioned materials, one of the experiment lines was dedicated to test the concept of a monitoring and actuation system developed in partnership with the University of Huddersfield. The scope of the system, not further discussed in this article, was to correct both dynamic and static deformations occurring in collimator jaws as a result of normal operation. The distortion detection of the impacted Al6082-T651 bars was performed resorting to optical fibres via dispersed reference interferometry (DRI). The actuation system, instead, was based on piezo-actuators, with a rise time in the order of μs, which is the period of flexural oscillations induced on the collimator jaw in case of beam impact [41].

As mentioned, the specimens were placed on graphitic elastic supports at the two extremities, with a contact pressure granted by springs with a spring ratio of 1 N mm^{-1} (Fig. 14). Graphite was chosen because of its transparency to the beam, for its mechanical damping properties and low shock impedance [42]. Modal analyses were also performed prior to the tests to calculate the numerical flexural frequency of each sample, and the results showed that, theoretically, the system was close to an ideal configuration of simple supports at each end. In fact, a transition between different boundary conditions was observed in some of the experimental responses [43]. The layout of the different target lines hosted within the rotatable barrel of the MultiMat test bench is reported in Table 3.

Experimental Protocol

Specimens were submitted to three different types of impacts: transversally-centred impacts, intermediate transversal offset and, where a coating was present, grazing impacts (Fig. 19).

Once the desired line was brought into impact position through a rotation of the barrel, the actual intensity, position and size of the shot pulses were measured resorting to BLMs and BTVs devices, with the beam size at the exact specimens position being derived resorting to the specification of HiRadMat beam optics. After impacts with high-intensity pulses, material lines were first brought into cool-down position, where a direct argon flow lowered their temperature, and then in inspection position, with the rad-hard camera spanning the overall length of the lines, thus allowing to visually check the status of the impacted specimens (Fig. 20).

The MultiMat experiment featured pulses of intensity ranging from one to 288 bunches, average bunch intensity of about 1.2×10^{11} protons per bunch (p/b) and beam size between 0.25 and 2 mm, as shown in Table 4. The intensity of the implemented beam pulses was progressively increased during the test, reaching energy densities $U_{\max}$ up to 10^4 J cm^{-3}.

The peak values of $\bar{U}_{\max}$ reached in MultiMat for various materials are compared in Table 5 to those foreseen in the relevant accidental scenario for collimation. In the case of graphitic materials, the design scenario is the HL-LHC beam injection error (BIE), where a full injection particle train (a total of 6.2×10^{13} protons, with an energy of 440 GeV) has a direct impact on the collimator jaw. For CuCD and heavier alloys, the design scenario involves the impact of one HL–LHC bunch on the material, taking place during an asynchronous beam dump (ABD).

This second scenario entails less energy on the target than the BIE. In Table 5, the parameters of the HL-LHC accidental scenarios and those of another experiment, HRMT23 [17], are reported. The HL-LHC scenarios leads to the most intense peaks of energy density $U_{\max}$ in bare materials, while with grazing pulses, with a smaller σ of 0.25 mm, even higher $U_{\max}$ values were achieved in MultiMat.

It was during MultiMat, however, that the maximum average energy densities $\bar{U}_{\max}$ were reached. In fact, in spite of the lower intensity beam pulses compared to HL-LHC BIE [5], the rod-like specimens impacted in MultiMat had a considerably smaller cross-sectional area, so that higher $\bar{U}_{\max}$ were achieved. Mechanical strains induced by these deposited energies could be preliminarily estimated thanks to the semi-analytical method presented in "Theoretical Considerations" section, making use of room-temperature thermophysical properties derived from [22]. It is interesting

Table 3 Layout of the specimens tested in the MultiMat experiment: coated samples are shown in bold characters

Line #	Specs	Slot#01 (125mm)	Slot#02 (125mm)	Slot#03 (125mm)	Slot#04 (125mm)	Slot#05 (125mm)	Slot#06 (125mm)	Slot#07 (125mm)	Slot#08 (125mm)
1	Material	**AC150K (CFC)**		AC150K (CFC)		AC150K (CFC)		AC150K (CFC)	
	Dim (x,y,z)	12x11.5x247 mm, 8 µm Mo		10x12x247 mm					
2	Material	Ti6Al4V	Ti6Al4V	Ti6Al4V		Ti6Al4V		IT180	IT180
	Dim (x,y,z)	10x10x121.75 mm						10x10x247 mm	
3	Material	CuCD – G2	CuCD – G2	CuCD – G2	CuCD – G2	CuCD – G2	CuCD – G2	CuCD – G2	CuCD – G2
	Dim (x,y,z)	10x10x120 mm							
4	Material	Al 6082-T651 (Huddersfield)				Al 6082-T651 (Huddesfield)			
	Dim (x,y,z)	10x10x490 mm							
5	Material	SiC		SiC		SiC		SiC	
	Dim (x,y,z)	10x10x247 mm							
6	Material	**MG6541Fc**	**MG6541Fc**	MG6541Fc	MG6541Fc	MG6541Fc	MG6541Fc	MG6541Fc	MG6541Fc
	Dim (x,y,z)	12x11.5x120 mm, 8 µm Mo		10x12x120 mm					
7	Material	CuCD – G1		CuCD – G1		CuCD – G1		CuCD – G1	
	Dim (x,y,z)	10x10x247 mm							
8	Material	**MG6403Fc**	**MG6403Fc**	MG6403Fc	MG6403Fc	MG6403Fc	MG6403Fc	MG6403Fc	MG6403Fc
	Dim (x,y,z)	12x11.5x120 mm, 5 µm TiN		10x12x120 mm					
9	**PARKING LINE**								
10	Material	Ta10W		Ta2.5W		Ta10W		Ta2.5W	
	Dim (x,y,z)	10x10x247 mm							
11	Material	TG-1100	TG-1100			CFOAM	CFOAM	CFOAM	
	Dim (x,y,z)	10x12x120 mm				10x10x247 mm			
12	Material	TG-1100	TG-1100	TG-1100	TG-1100	TG-1100	TG-1100	NNK265-266	NNK265-266
	Dim (x,y,z)	12x11.5x120 mm		10x12x120 mm				10x12x120 mm	
13	Material	TPG		TPG		TPG		TPG	
	Dim (x,y,z)	7x8x247 mm							
14	Material	TZM		TZM		TZM		TZM	
	Dim (x,y,z)	10x10x247 mm							
15	Material	**R4550**		R4550		R4550		R4550	
	Dim (x,y,z)	12x11.5x247 mm, 2 µm Cu		10x12x247 mm					
16	Material	**MG6530Aa**	**MG6530Aa**	MG6530Aa	MG6530Aa	MG6530Aa	MG6530Aa	MG6530Aa	MG6530Aa
	Dim (x,y,z)	12x11.5x120 mm, 2 µm Cu		10x12x120 mm					

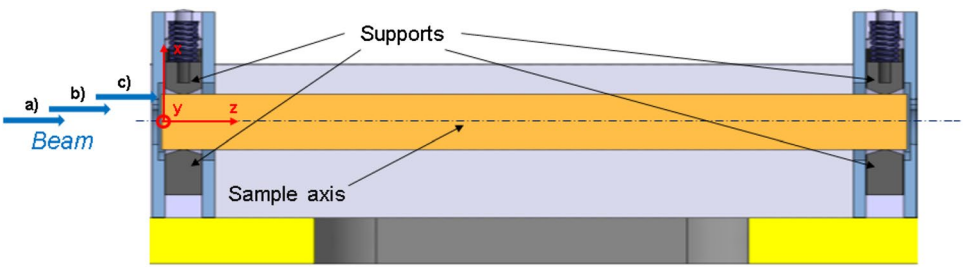

Fig. 19 The different types of impacts implemented in MultiMat described with respect to the specimen reference frame shown in figure: centred pulses (*a*), off-axis pulses (*b*) and grazing pulses (*c*)

to note that, for MoGr, mechanical strains in the direction normal to the basal planes were expected to exceed admissible limits calculated in quasi-static conditions (ε_{lim}).

The specimen aspect ratio allowed generating signals in which the footprint of different phenomena, at distinct timescales, could be easily detected. In the first 1–10 µs, a signal rise time, associated to the pulse duration, occurred: in this phase, the highest strain rates were attained, with values as high as 10^4 s^{-1}; transversal waves were also excited, with periods of several microseconds; these were particularly appreciable in those materials having slow transverse speed of sound, such as anisotropic materials. Subsequently, a longitudinal wave, with a period in the order of 100 µs, was generated: this regime proved to be particularly useful

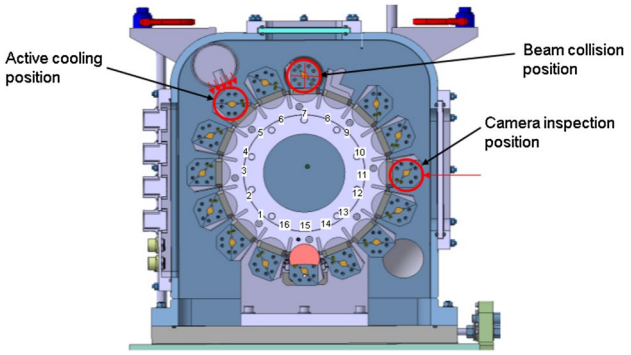

Fig. 20 Schematic representation of the interior of the MultiMat aluminium tank: the beam collision position, the active cooling station and the inspection position are shown

to study material elastic constants, internal damping and axial strength. In case of off-centre beam impacts, bending oscillations were additionally induced: these had a period in the range of 1 ms and were useful to determine the flexural strength, plasticity and low-frequency damping. Finally, temperature evolved on a significantly longer timescale, 0.1 s or more for the considered dimensions: this is why most of the dynamic phenomena could be reasonably considered as quasi-instantaneous and adiabatic.

Numerical and Experimental Results

In this section, some of the most significant results obtained benchmarking numerical simulations with experimental data are presented.

Impacts on Bare Samples

CFC Samples

Figure 21a shows the temperature profile induced over the fourth sample (the most loaded one, see Fig. 22) of the CFC AC150 K line at the end of an impact with a 36 bunches-pulse, intensity 1.24×10^{11} p/b and $\sigma=0.5$ mm. A maximum temperature of about 114 °C is reached at the end of the energy deposition time, i.e. $\tau=900$ ns, decreasing to $T_f=38.1$ °C after about 2 s and then remaining almost constant, as no convection was considered in the simulation.

Table 4 Beam parameters during the MultiMat test run: number of delivered pulses P, number of bunches per pulse b, average intensity I, beam size σ. A total of 478 pulses (2.25×10^{15} p) were shot from 2 to 17/10/2017

Material	P #	b #	I [p/b]	σ [mm]	Material	P #	b #	I [p/b]	σ [mm]
IT180	9	1–24	1.1×10^{11}	2	MG6530Aa	46	1-288	1.3×10^{11}	0.25, 0.5
Ta10 W	7	1–24	1.2×10^{11}	2	MG6541Fc	42	1–288	1.3×10^{11}	0.25, 0.5
Ta2.5 W	7	1–24	1.2×10^{11}	2	TPG	21	1–24	1.1×10^{11}	2
TZM	50	1–36	1.3×10^{11}	0.5, 2	TG1100	28	1–288	1.3×10^{11}	0.25, 0.5
CuCD-G2	30	1–24	1.1×10^{11}	0.5, 2	R4550	47	1–288	1.2×10^{11}	0.25, 0.5
CuCD-G1	17	1–24	1.4×10^{11}	0.5	CFC-AC150 K	32	1–288	1.2×10^{11}	0.25, 0.5
SiC	81	1–24	1.1×10^{11}	0.5, 2	Ti6Al4 V	9	1–24	1.1×10^{11}	2
MG6403Fc	40	1–288	1.3×10^{11}	0.25, 0.5	CFOAM	8	144–288	1.2×10^{11}	0.25, 0.5
NNK265-266	28	1–288	1.3×10^{11}	0.25, 0.5	Al6082-T651	8	24–72	1.1×10^{11}	2

Table 5 Maximum values of the average energy density $\bar{U}_{\max}$ and temperature $\bar{T}_{\max}$ on the bulk of different materials predicted by simulations for MultiMat (M) experiment compared to those foreseen for HL-LHC BIE (HL) and achieved in HRMT23 (J). The associated temperatures achieved at the end of the beam pulse $\bar{T}_{\max}$ as well as the maximum longitudinal and transverse strains are also reported, based on thermophysical properties presented in [22]. In case of anisotropic materials, e.g. MoGr and CFC, values in the transverse direction refers to direction normal to the basal planes

	$\bar{U}_{\max}$ (kJ cm^{-3})			$\bar{T}_{\max}$ (°C)			$\varepsilon_L=2\alpha_L\bar{T}_{\max}$ ($\mu\varepsilon$)			$\varepsilon_T=2\alpha_T\bar{T}_{\max}$ ($\mu\varepsilon$)			ε_{lim} ($\mu\varepsilon$)	
	HL	M	J	HL	M	J	HL	M	J	HL	M	J	L	T
MG6403Fc	0.46	0.97	0.28	167	353	102	860	1813	523	2870	6053	1747	1960	5140
MG6530Aa				170	358	103	554	1169	337	4182	8818	2545		
MG6541Fc				169	357	103	650	1371	396	3454	7283	2102		
NNK265-266		0.87		167	316	102	519	981	316	4617	8732	2810		
AC150 K	0.10	0.27	0.08	52	142	42	−105	−283	−84	1132	3058	906	1470	3820
R4550	–	0.31	–	–	155	–	–	1319	–	–	1319	–	7153	7153
CuCD	0.15	0.47	0.46	53	167	163	850	2650	2594	850	2650	2594	5750	5750

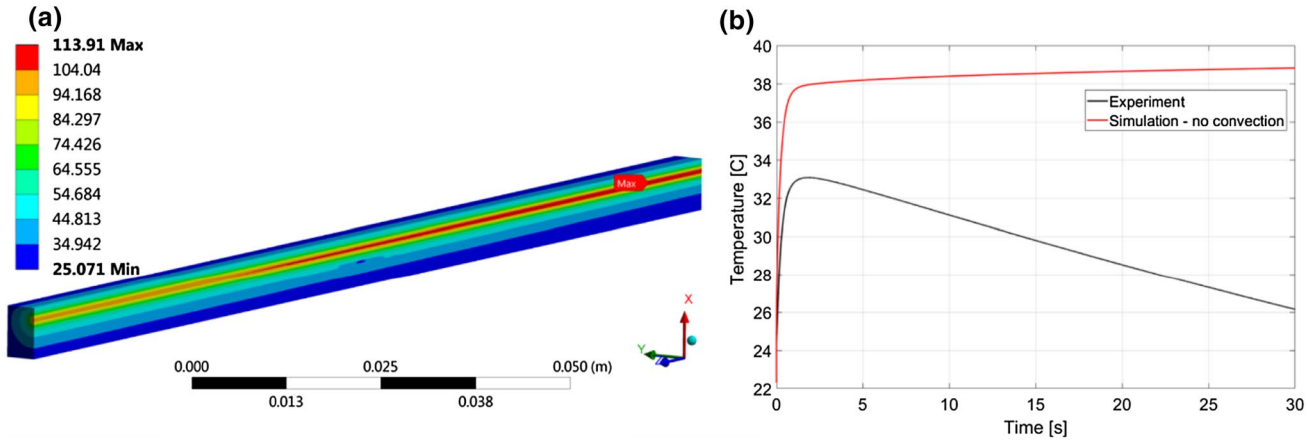

Fig. 21 The temperature field over the fourth CFC AC150 k specimen impacted by a 36 bunches-pulse with bunch intensity of 1.24×10^{11} p/b, $\sigma=0.5$ mm and 2.7 mm x-wise offset (**a**); a comparison between the experimental and the (minimum) simulated temperature acquired at the midpoint of its bottom face is also shown (**b**)

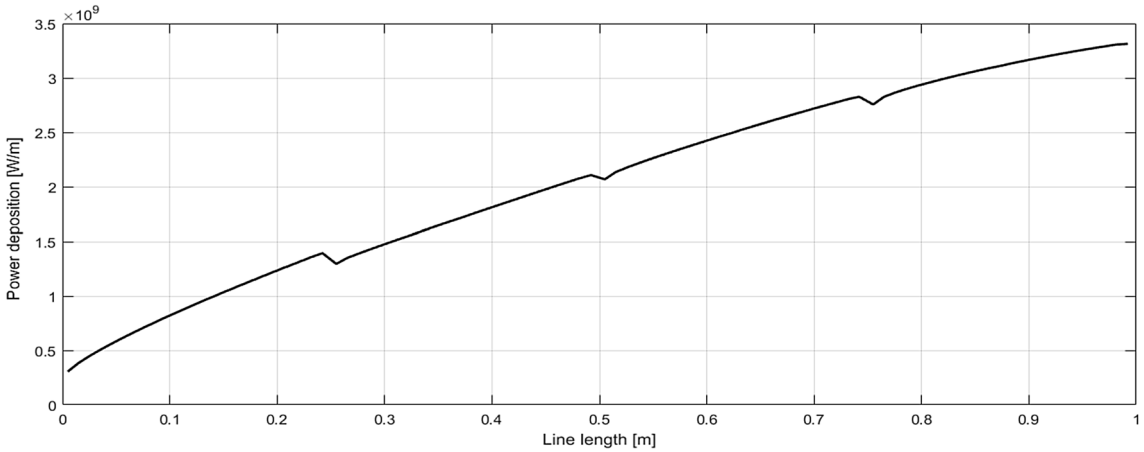

Fig. 22 The power distribution over the four CFC AC150 K samples of line 1 (see Table 3) due to a 36 bunches-pulse with bunch intensity of 1.24×10^{11} p/b and $\sigma=0.5$ mm

A comparison with the experimental temperature reported in Fig. 21b, reveals a peak of temperature of $T_{peak}=33.1$ °C after 1.7 s, in acceptable agreement with the numerical simulation, particularly taking into account the thermal impedance between the Pt100 probe and the sample as well as the convection (natural and/or forced). The subsequent temperature decrease is due to the argon-based cooling system installed in the experiment. This result confirms the accuracy of the values of specific heat c_p in temperature implemented in the simulations. The transverse (i.e. along the direction normal to basal planes, or x according to the specimens layout reported in Fig. 19) and longitudinal total strains induced by a 288 bunch-pulse are shown in Fig. 23. A very close agreement between numerical and experimental data is found both in terms of amplitude and of frequencies (16.3 kHz and 66.7 kHz for the experimental longitudinal and transverse strains, 16.4 kHz and 70.5 kHz for their numerical counterparts, respectively). These values agree well with the theoretically predicted longitudinal strains (-283 μm m^{-1}), while transverse strains are significantly lower than the 3000 μm m^{-1} reported in Table 5.

A Rayleigh damping ratio of $\zeta=0.001\%$ at 65 kHz was also found for transverse strains. As expected, transverse strains assume values which are much larger than the longitudinal strains, this being due to both a larger CTE in the x direction ($\sim10^{-5}$ °C^{-1} vs. $\sim10^{-6}$ °C^{-1}) and a smaller Young's modulus (3.1 GPa vs. 110.2 GPa). It is worth remarking that the longitudinal strains are, in fact, negative, as AC150 K has a negative CTE in the axial direction. This means that the quasi-instantaneous heat deposition associated to the impact makes the specimen willing to shrink in that direction, being prevented to do so by inertia, resulting then in a

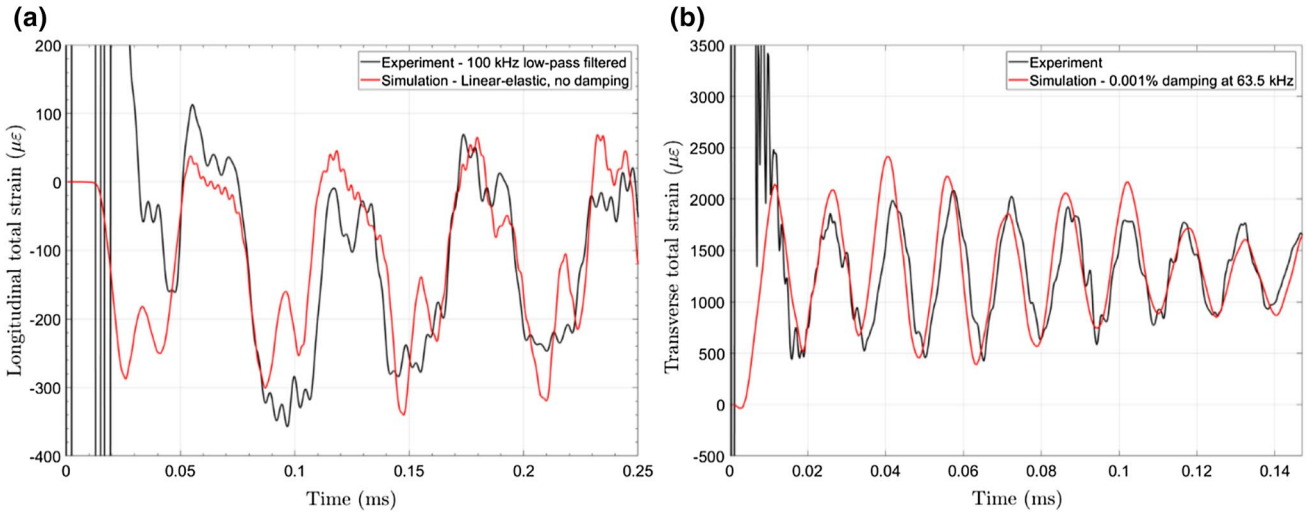

Fig. 23 The numerical and experimental longitudinal (**a**) and transverse (**b**), i.e., normal to basal planes, total strains acquired on the fourth CFC AC150 K sample subject to a centred 288 bunches-pulse with intensity 1.27×10^{11} p/b and $\sigma = 0.5$ mm

state of tension. This is confirmed by simulations: Fig. 24a shows that during the 288 bunches-pulse, the impacted portion of the specimen is in tension, while compression occurs in the outer regions of the sample.

Molybdenum–Graphite Samples

A more canonical behaviour than the one observed for CFC AC150 K is found for the first MoGr NNK265-266 sample. In this case, in fact, the centred 288 bunches-pulse with 1.23×10^{11} p/b and $\sigma = 0.5$ mm provokes a state of compression about the sample axis during the impact, while the surrounding areas experience tension, as clearly visible in Fig. 24b. As discussed in "Dynamic Response of Materials Subject to Quasi-Instantaneous Heating" section, two tensile waves then rise at the free end faces of the NNK265-266 sample in order to fulfil the boundary conditions in the longitudinal direction, then propagating towards the opposite face and superimposing along the specimen's length, as shown in Fig. 25a. Here a close correlation is found between simulated and actual longitudinal total strains acquired at the midpoint of the right surface of the specimen, with a numerical value of the longitudinal wave frequency of 22.5 kHz, against an experimental value of 21.8 kHz. Also in this case a linear elastic constitutive model was implemented, with a Rayleigh damping ratio of $\zeta = 0.0075\%$ found at 22.5 kHz. The maximum amplitude of the first longitudinal strain wave of 825 μm m^{-1} shown in Fig. 25a is smaller than the

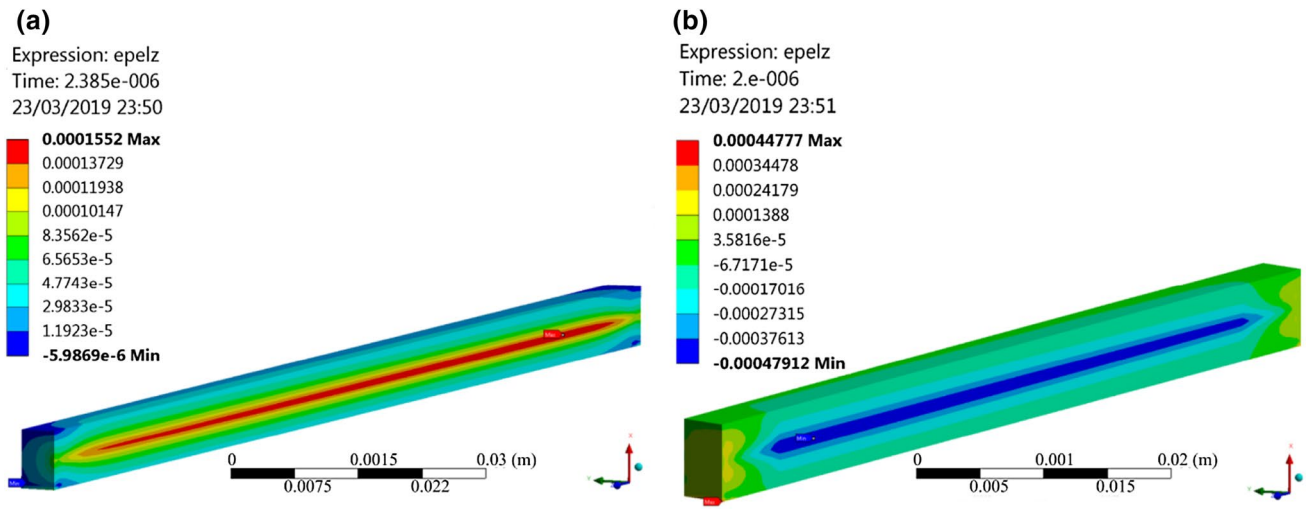

Fig. 24 The longitudinal mechanical strain occurring after a 288-bunch pulse impacting a CFC AC150 K sample (**a**) and a MoGr NN265-266 sample (**b**)

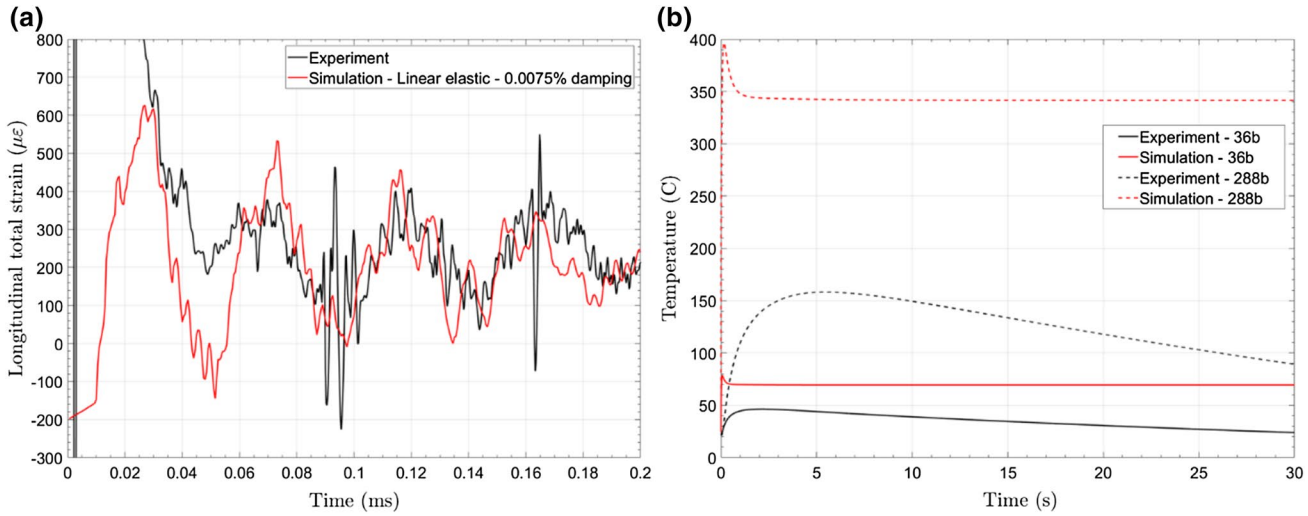

Fig. 25 The longitudinal total strain occurring on the first NNK265-266 sample impacted by a 288 bunches-pulse with intensity 1.23×10^{11} p/b and $\sigma = 0.5$ mm (**a**). The measured and simulated maximum temperature over time for the same 288 bunches-pulse and for a 36 bunches-pulse impacting the second NNK265-266 sample of line 12 (see Table 3)

predicted 981 μm m^{-1} of Table 5. This is due to the fact that the NNK265-266 specimen here considered is not the most loaded of the line (the second one), to which the value of Table 5 is referred.

For the present sample, in fact, $\bar{U}_{max} = 0.79$ kJ cm^{-3}, leading to a maximum theoretical amplitude of the strain wave of 891 μm m^{-1}: this value would go down to about 850 if damping were also considered.

Figure 25b shows the variations in time of the maximum temperature occurring on the second NNK265-266 sample of line 12 (see Table 3) for the 288-bunch pulse and for a less intense 36-bunch pulse. The second NNK265-266 samples is analysed as no temperature probe survived to the impacts on the first specimen. From the plot it can be observed that a considerable difference exists between numerical and experimental values already for the 36-bunches pulse. This deviation becomes even larger for the case of the impact with 288 bunches: here the measured temperatures exceed 155 °C, which is the specified limit temperature for the adhesive bonding the probe to the sample, as discussed in "Experiment Description" section. The good matching between numerical predictions and strain measurements seems to point to a strong underestimation of the temperature measure, possibly due a partial detachment of the sensor from the sample.

As found for CFC AC150 K, also for MoGr transverse strains assume values that are much larger than their longitudinal counterpart. This can be easily observed in Fig. 26a, where the numerical total transverse strains induced by a 288-bunches pulse in the most loaded samples of different MoGr grades and in CFC samples are reported for the sake of comparison. Differences between MoGr grades are essentially due to the variations in the transversal CTE between them. The lower total strain in CFC is due to the significantly lower energy deposited on this material.

Figure 26b shows also the mechanical strains, proportional to thermal stresses, probed at the midpoint of the lateral faces of the samples. It is interesting to see how the MoGr peak values agree well with the theoretical predictions of Table 5 of about 7000 με. An exception is constituted by the simulated NNK265-266 sample, which was not the most loaded specimen of the line (on that specimen all strain gauges detached because of the temperature so that no measure was available for the pulse of interest).

Graphite Samples

The longitudinal total strain acquired on the outer surface of the most loaded R4550 sample impacted by a centred 288 bunches-pulse having average intensity of 1.25×10^{11} p/b and $\sigma = 0.5$ mm sigma is shown in Fig. 27a. A deviation between numerical and experimental data is observed in terms of amplitude and frequency: a subsequent 6% reduction of the Young's modulus implemented in the considered linear elastic constitutive law, allowed achieving a better correlation. Moreover, a Rayleigh damping ratio of $\zeta = 3\%$ was implemented.

Observing Fig. 27a it is possible to notice that in R4550 longitudinal strain waves feature a quite regular step-like shape, with minor effects due to coupling with radial waves. In fact, the simulated dynamic component of the total transverse strain shown in Fig. 27b is small, the overall strain oscillating slightly about its static value. This behaviour is due to the fact that the energy deposition time

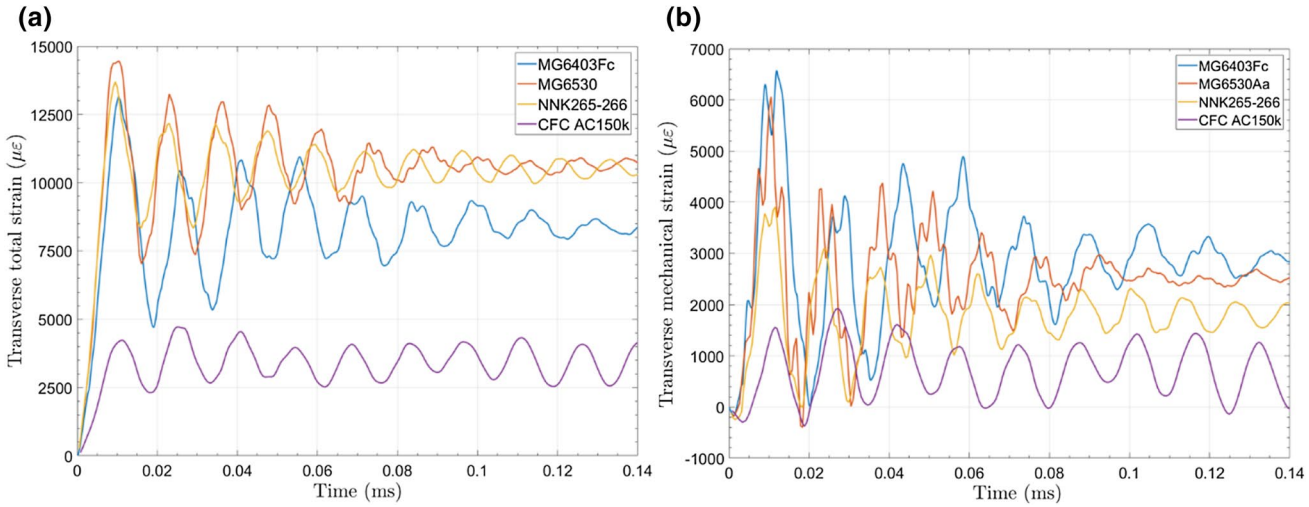

Fig. 26 Simulated transverse total strains (**a**) occurring on the core of the most loaded sample of various MoGr grades (NNK265-266, MG6403Fc and MG6530Aa) and of CFC AC150 K impacted by a 288-bunch pulse with average intensity of 1.25×10^{11} p/b and $\sigma=0.5$ mm; the numerical mechanical strains arising on the lateral faces of the same samples are shown in (**b**)

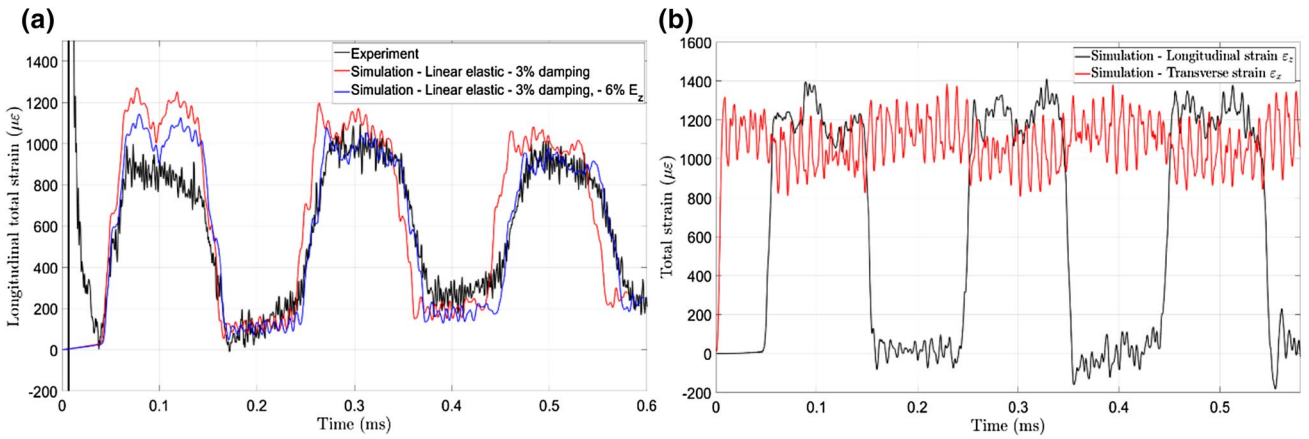

Fig. 27 The longitudinal total strains (**a**) occurring on the outer surface of the most loaded R4550 sample impacted by 288 bunches of intensity 1.25×10^{11} p/b and $\sigma=0.5$ mm. The undamped numerical longitudinal and transverse total strains are shown in (**b**)

$\tau=7.95$ μs is very close to the radial waves propagation period $\Gamma_r=7.88$ μs.

As seen in "Dynamic Response of Materials Subject to Quasi-Instantaneous Heating" section, in this condition stress relaxation in transverse direction takes place while energy is still being deposited, leading to a significant reduction of the dynamic component of transverse stresses. This dynamic component of stress is however expected to fully develop in larger cross-sections, such as in a collimator jaw, having longer transverse wave periods.

Copper–Diamond Samples

The case of CuCD-G1 line impacted by a 1-buch pulse having intensity of 1.43×10^{11} protons, $\sigma=0.5$ mm sigma and an offset of 3.1 mm in x-direction is analyzed on the most loaded sample.

Having an only limited knowledge of the Young's modulus of this specific material grade, the mechanical problem is tackled estimating such value from the frequency exhibited by the experimentally measured longitudinal wave, namely E = 208 GPa. As additional mean of comparison, an elasto-plastic model based on the measures carried out for a similar CuCD grade (namely, CuCD 40/60 [44]) was also implemented.

Figure 28a, b show the propagation of longitudinal waves though the midpoint of the bottom face of the sample: while the elastic model seems to better match the experimental period, on the other hand the elasto-plastic counterpart appears to be able to mimic the amplitude of the higher frequency content of the signal. The bending oscillations associated to the same pulse are shown in Fig. 28c, d. In the former, a comparison between the purely elastic and elasto-plastic models with respect the experimental data is provided, while the latter reports the numerical results with the addition of damping in the elasto-plastic case. A Rayleigh $\zeta = 8\%$ damping ratio is also introduced, estimated via logarithmic decrement from the experimental flexural oscillations.

TaW, IT180, TZM and SiC samples

As mentioned in "Overview of Tested Materials" section, different heavy alloys were tested in MultiMat, as tantalum- (Ta10/2.5 W) and tungsten-based (IT180) materials.

The first sample of the TaW line (i.e. a Ta10W-made specimen, as reported in Table 3), given the material's density, results to be the most loaded one when impacted by a 2-bunches pulse having intensity of 2.19×10^{11} p/b, $\sigma = 2$ mm sigma and an x-wise offset of 2.2 mm with respect to the sample axis, resulting into a maximum beam-induced ΔT of about 380 °C. The longitudinal total strain at the middle of the sample bottom face is shown in Fig. 29a: the numerical response is obtained via a purely elastic constitutive law. The propagation of a classical step-shaped longitudinal wave can be clearly seen. A good agreement between experimental and numerical results is noticeable both in terms of amplitudes and frequency content (6.6 kHz

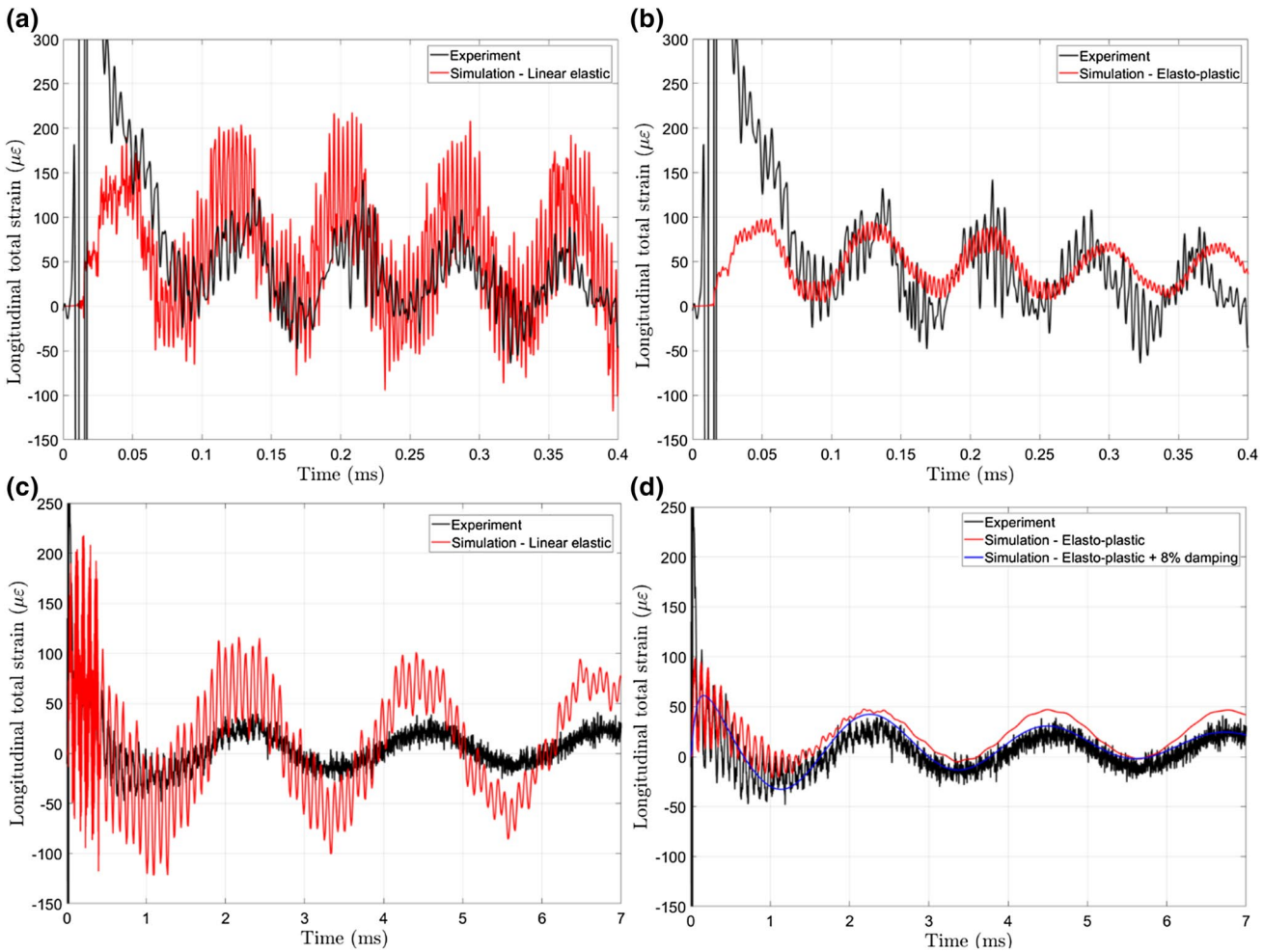

Fig. 28 The longitudinal total strain occurring on the second sample of the CuCD-G1 line impacted by a 1 bunch-pulse with intensity 1.43×10^{11} p, $\sigma = 0.5$ mm and an x-wise offset of 3.1 mm with respect to the sample's axis. The strain associated to the propagation of longitudinal waves is shown for the case of a linear-elastic (**a**) and elasto-plastic (**b**) constitutive model. Flexural oscillations are shown instead in (**c**) and (**d**)

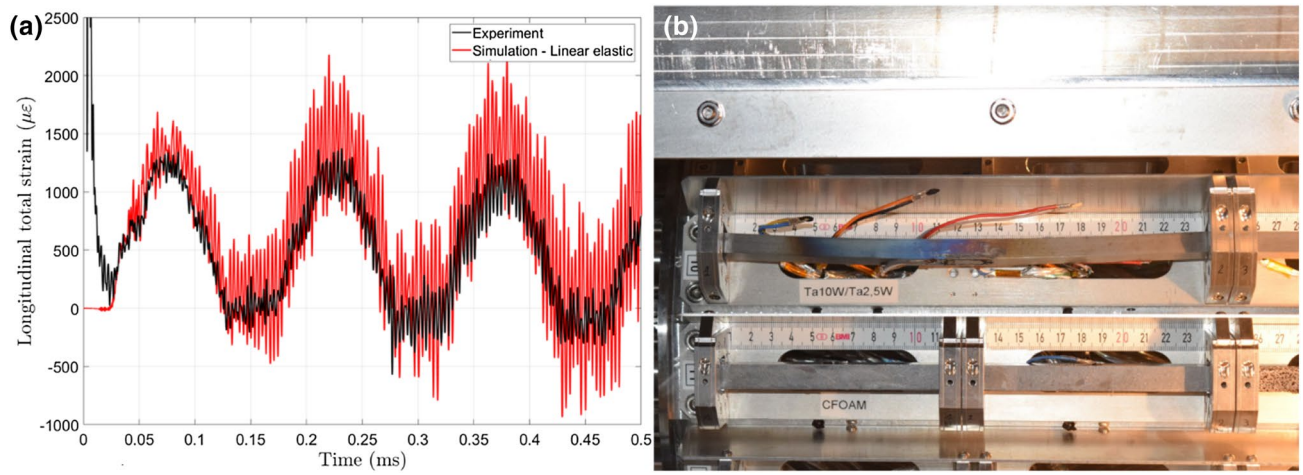

Fig. 29 The simulated longitudinal total strains occurring at the midpoint of the bottom face of a Ta10W sample impacted by a 2-bunches pulse with intensity of 2.19×10^{11} p/b and $\sigma=2$ mm (**a**); the plastic deformation induced by a subsequent 24 bunches-pulse impacting the same sample is shown in (**b**)

vs. 7.1 kHz for the simulated response). The effects of a subsequent 24 bunches-pulse impacting the same sample are shown in Fig. 29b: a clear plasticization of the specimen is visible. The planned post-mortem tests, as tomography, which are currently ongoing on the impacted specimens, will allow gaining further insight about their state of integrity.

Similar investigations are performed for the first IT180 sample of line 2 (see Table 3). Given a density of 18 g cm^{-3}, this sample is the most loaded of its line when impacted by a 1-bunch pulse having intensity of 2.03×10^{11} p/b, $\sigma=2$ mm sigma and x-wise offset of -3 mm with respect to the sample axis, inducing a maximum ΔT of about 206 °C. The longitudinal total strain at the middle of the sample bottom face is shown in Fig. 30a: the numerical response is obtained via an elasto-plastic constitutive law. Good correlation between experimental and numerical results is observable both in terms of amplitudes and frequency content (9.1 kHz vs. 9.3 kHz for the simulated response). The amplitude of high frequency content in the axial response, mainly due to radial wave propagation, is larger in the simulated response. For this reason, a Raleigh damping ratio of $\zeta=1\%$ associated to the frequency of radial waves is adopted: in this case, however, the numerical signal seems to be too much damped with respect to its experimental counterpart, suggesting that an actual damping value smaller than 1% is present. As done for Ta10 W, also here a clear plasticization of

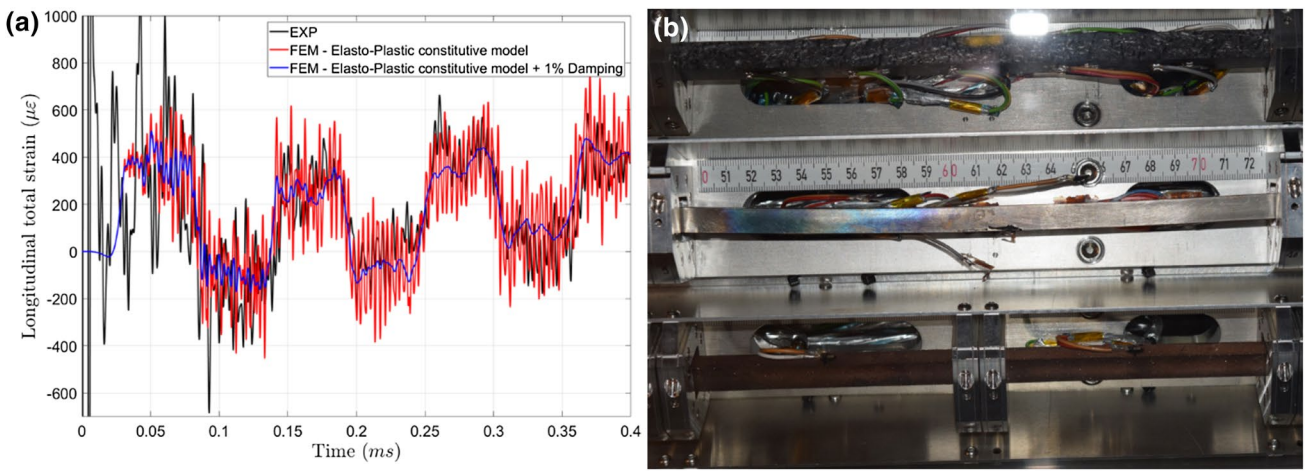

Fig. 30 The simulated longitudinal total strains occurring on midpoint of the bottom face of an IT180 sample impacted by a 1-bunch pulse with intensity of 2.03×10^{11} p/b and $\sigma=2$ mm (**a**); the plastic deformation induced by subsequent 12 and 24 bunches-pulses impacting the same sample is shown in (**b**)

the specimen due to higher-intensity pulses is reached, as visible in Fig. 30b.

In fact, also the failure of different specimens was clearly observed during the experiment: this is the case of SiC and TZM samples, as shown in Fig. 31. A study aimed at gaining insight on the physics involved in such damage scenarios is currently ongoing [43].

Grazing Impacts on Coated Samples

A series of grazing impacts were carried out on coated samples to probe the coatings strength, their adhesion to the substrates and to verify the extent of the induced surface damages in case of accidental scenarios. In this phase of the tests, energy deposition densities exceeded those associated to the HL-LHC BIE, by strongly focusing the beam, as shown in Table 6. Under these conditions, the induced temperatures were expected to cause coating melting and ejection.

As discussed in "Dynamic Response of Materials Subject to Quasi-Instantaneous Heating" section, to correctly simulate such phenomena, the adoption of appropriate equations of state, strength and failure models would be required, together with the use of suitable explicit code. Nonetheless, preliminary thermal studies were carried out resorting to the ANSYS implicit solver in order to get a first approximation of the temperatures reached during the impacts. The smallest available nominal beam size of $\sigma = 0.25$ mm and the highest bunch intensity of 1.4×10^{11} p/b were implemented for the tests to mimic or, as it was the case, to exceed HL-LHC BIE energy densities. The samples were impacted 150 µm and 500 µm beneath the coated surface. A double alignment of the targets was carried out resorting to both BTVs and BLMs. In addition to this, the average x-wise offset of the coated surface of each samples as well as the planarity of the overall line to be impacted was estimated resorting to metrology measures (Fig. 32).

The effects of the pulses shot on coatings are shown in Fig. 33, together with the beam parameters. As expected, it can be observed that copper-coated specimens exhibit a much more visible damage with respect to those samples which feature a coating in molybdenum, this being mainly due to copper lower melting temperature ($T_m^{Cu} = 1085$ °C vs. $T_m^{Mo} = 2623$ °C). Larger damage stripes (up to 1.9 mm) are therefore visible on Cu-coated samples, this also being due in part to the smaller impact factors implemented with respect to Mo-coated samples, as both 150 µm and 500 µm were considered for the latter, while only 150 µm were taken into account for the others.

Numerical simulations show that only a portion of the damages observable in Fig. 33 are due to material melting. The case of MG6541Fc coated with Mo is presented in Fig. 34: a maximum temperature of $T_{max}^{Mo} = 2845$ °C is found. In Fig. 34a, the portion of the specimen undergoing

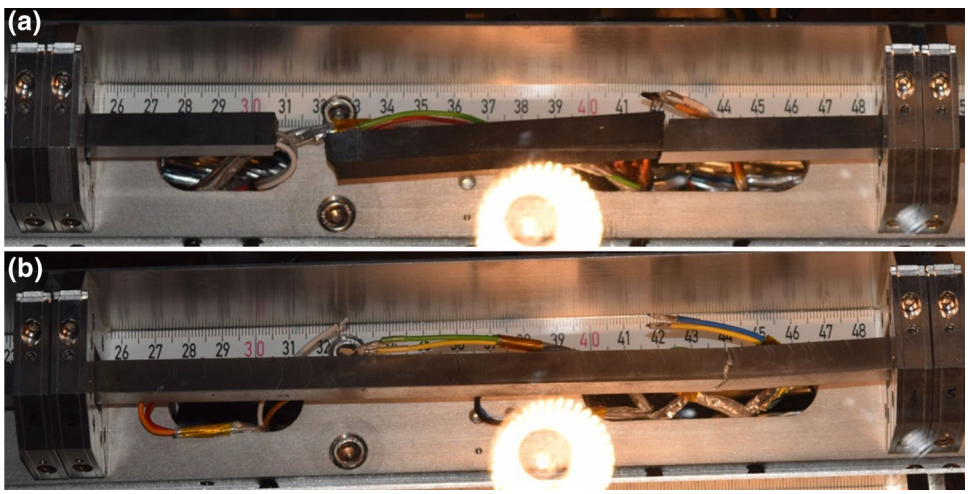

Fig. 31 The beam-induced failure of the second SiC sample of line 5 and of the second TZM sample of line 14, impacted by a 36 bunches-pulse with 1.18×10^{11} p/b and $\sigma = 0.5$ mm and by a 12-bunches pulse with 1.33×10^{11} p/b and $\sigma = 2$ mm, respectively

Table 6 Beam parameters of the most energetic pulses delivered during the MultiMat test run compared to the energy densities typical of the HL-LHC Beam Injection Error (BIE) scenario [5]

Material [sub-coat]	Intensity [10^{13} p]	Impact parameter [um]	σ(x,y) [mm]	U_{max} coating [kJ cm^{-3}]	U_{max} substrate [kJ cm^{-3}]	U_{max} HL-LHC (BIE) [kJ cm^{-3}]
MG6541Fc- Mo	3.66	− 150	0.29 × 0.31	13.85	6.11	6.09
MG6530 - Cu	3.99	− 150	0.29 × 0.26	15.31	7.68	
AC150 K - Mo	3.68	− 150	0.38 × 0.23	14.27	3.72	2.55
R4550 - Cu	4.04	− 150	0.31 × 0.27	12.30	4.15	–

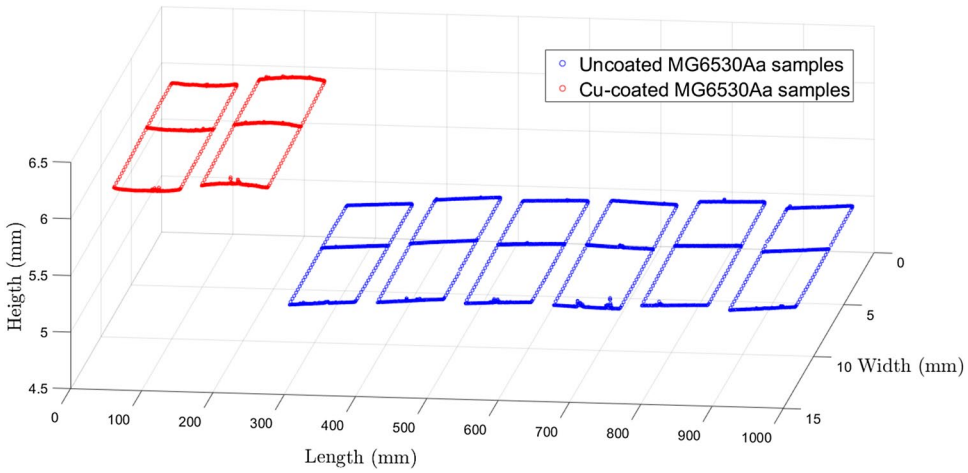

Fig. 32 Metrology measures of the top surfaces of the MG6530Aa samples

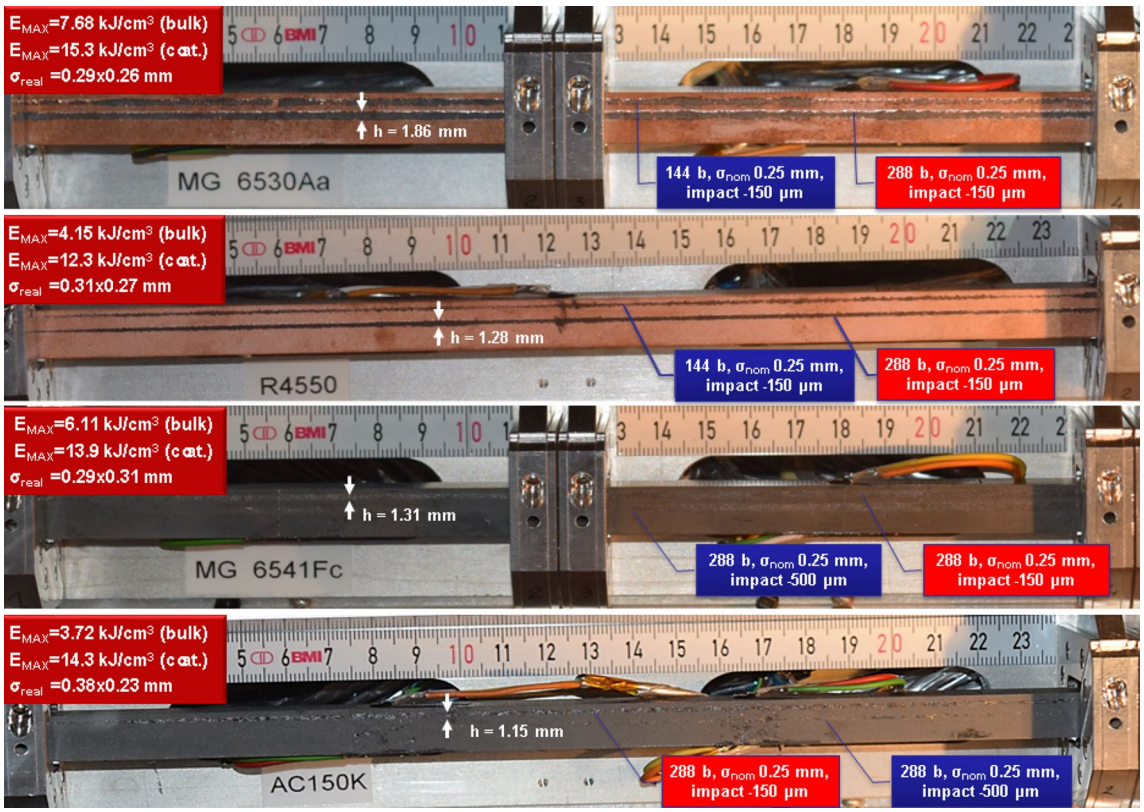

Fig. 33 The effects of grazing pulses on Cu and Mo coatings, together with the implemented beam parameters

temperatures higher than molybdenum melting temperature $T_m^{Mo} = 2623$ °C is shown in red: only 55.9 mm of the 120 mm-long damage stripe observed in Fig. 33 experience melting, indicating the occurrence of micro-jetting and spallation in the remaining areas. A similar result is highlighted in Fig. 34b, with a melted width of 0.32 mm out of the 1.31 mm found in Fig. 33.

Post-irradiation Analyses

After the completion of the tests on October 2017, the MultiMat test-bench was transferred to a storage area and then opened on February 2019, once the dose rate reached a few µSv/h. After a first visual inspection of the components non-destructive investigations were started.

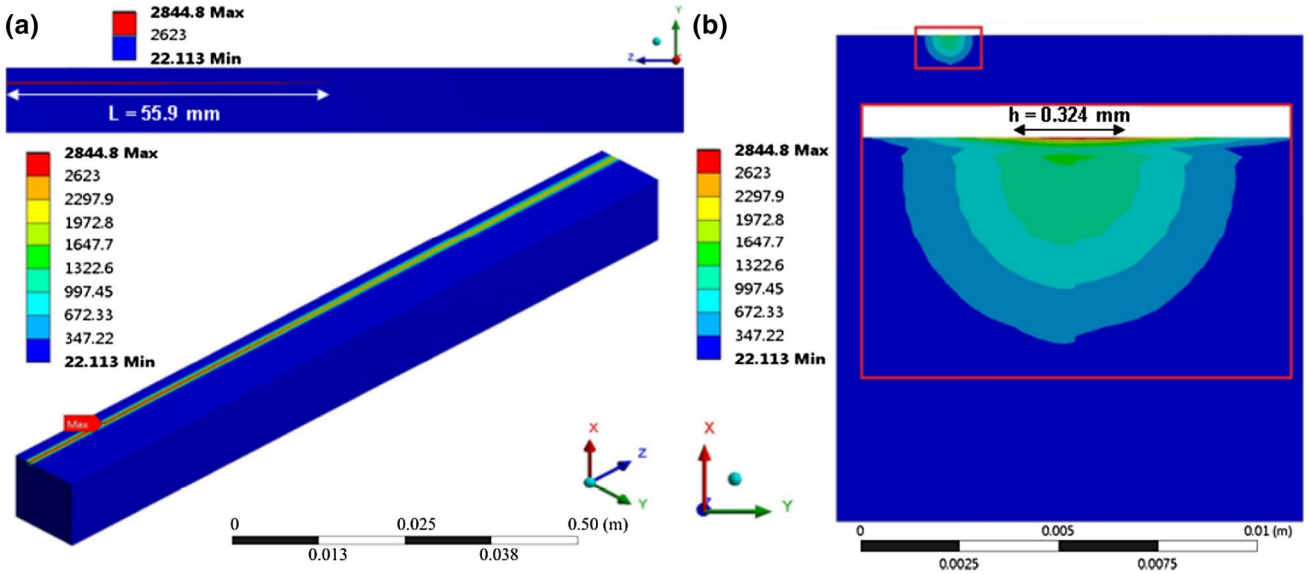

Fig. 34 The simulated grazing impact of a 288-bunch pulse with intensity 1.27×10^{11} p/b and $\sigma=0.25$ mm over the molybdenum coating of a MG6541Fc sample. Melted portion of the coating are shown in red

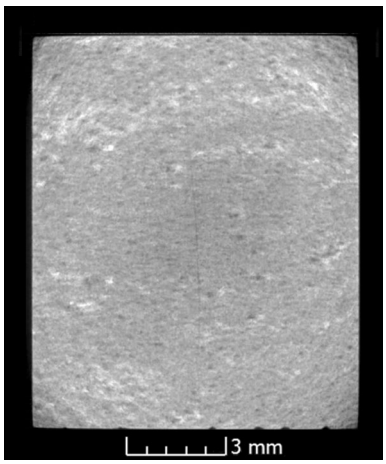

Fig. 35 Computed tomography scans over the transverse cross-section of the most loaded samples of MG6403Fc, showing cracks developing in direction parallel to the basal plane

A tomography campaign aimed at evaluating the state of integrity of the impacted samples confirmed the theoretical results predicted in Table 5.

The most loaded samples of the MoGr grades, which had attained thermomechanical loads a factor of two to three higher than those expected in the worst HL-LHC accident scenario, showed signs of onset of mechanical damage, while maintaining the global structural integrity of the sample, as shown for instance in Fig. 35. Some cracks, which started from the lateral faces and propagated towards the core of the sample, caused a local delamination between adjacent basal planes. Cracks were more evident in the samples that experienced repeated pulses at the highest intensity, thereby fostering crack propagation. In the case of use in a collimator, this local damage would not affect the collimator functionality: we can hence conclude that the safety margin with respect to the worst accidental scenario for HL-LHC collimator for MoGr is at least of a factor of two.

CFC AC150 K and isotropic graphite R4550, which attained lower average energy densities (Table 5), did not reveal evidence of cracks, in line with predictions.

CuCD specimens, subject to less intense pulses (up to 24 bunches with $\sigma=0.5$ mm), did not show presence of damages after the first visual inspections (to be confirmed by ongoing tomography tests).

Finally, failure on YZ planes due to crack propagation was also found on the most loaded SiC and TZM samples, which were already seen showing macroscopic failure in the transverse cross-section due to longitudinal stresses (Fig. 36).

Conclusions

The study of the dynamic phenomena generated in matter when impacted by energetic particle beams can be performed resorting to numerical approaches. However, the constitutive models required to perform such simulations, at the extreme conditions, as to temperature, pressure and density, induced by such impacts, are hardly available in scientific literature. With these limitations in mind, a number of dedicated tests in experimental facilities using intense and

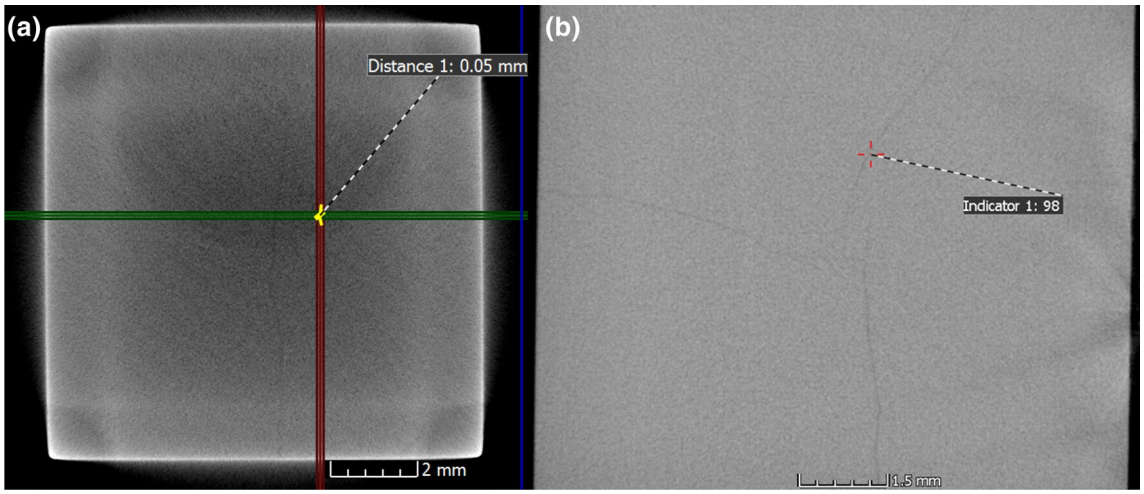

Fig. 36 Computed tomography scans over the transverse cross-section of the most loaded samples of TZM (**a**) and SiC (**b**)

energetic particle pulses were carried out over the years, with the goal of deriving or validating material models, exploring regions in the materials state diagram (pressure, density, internal energy) which cannot be attained through traditional dynamic tests,

The MultiMat experiment was performed in October 2017 at CERN HiRadMat facility with the goal of gathering experimental data upon which building or validating reliable constitutive models for a wide variety of materials meant to be used in beam-interacting devices, particularly collimators, subjected to potentially destructive events caused by the impact of energetic particle beams.

In total, 81 samples in the form of slender rods were tested: their geometry had cross sections varying from 7×8 mm^2 to 12×11.5 mm^2 and lengths of 120 mm or 247 mm. Specimens were made out of 18 different materials, ranging from very low-density carbon foams to heavy materials as TZM molybdenum, tantalum-tungsten and tungsten heavy alloys; some of the carbonaceous samples were coated with molybdenum, copper and TiN thin films.

The behaviour of the tested samples was monitored online relying on embarked sensors (335 strain gauges and 112 thermal probes) and remote instrumentation, namely a Laser Doppler Vibrometer (LDV). Intensities, profiles and frequencies of the stress waves measured on the outer surfaces of the samples were benchmarked against those predicted by numerical simulations.

Specimens were submitted to three different types of impacts: axially centred impacts, intermediate offset and, where a coating was present, grazing impacts. The specimens aspect ratio allowed generating signals in which the footprint of different phenomena, at distinct timescales, could be easily detected. In the first 1–10 μs, a signal rise time, associated to the pulse duration, occurred: in this phase, the highest strain rates were attained, namely in the transverse directions, with values as high as 10^4 s^{-1}; transversal waves were also excited, with periods of several microseconds. Subsequently, a longitudinal wave, with a distinct trapezoidal pattern and a period in the order of 100 μs, was generated: this regime proved to be particularly useful to study material elastic constants, internal damping and axial strength. If the impact was transversely offset, lateral oscillations were also excited: these had a period in the range of 1 ms and were useful to determine the flexural strength, plasticity and low-frequency damping. Finally, temperature evolved on a significantly longer timescale, 0.1 s or more for the considered dimensions: this is why most of the dynamic phenomena could be reasonably considered as quasi-instantaneous and adiabatic.

During the test, beam pulse intensity ranged from one to 288 particle bunches, with average bunch intensity of about 1.2×10^{11} protons per bunch and beam sizes as small as 0.25 mm, allowing to reach peak energy densities up to 10^4 J cm^{-3}, in excess of those expected in the HL-LHC worst accidental scenarios.

One of the main innovative features of the experiment was the ability, thanks to the focusing effect allowed by the rod slender geometry, to achieve stresses and strains, in some cases, largely above those expected in case of accidents on collimators for the High Luminosity upgrade of the LHC (HL-LHC), with a pulse intensity significantly lower. More than twice the values expected in HL-LHC were reached in MultiMat for all molybdenum–graphite grades and CFC. This constituted one of the main achievements of the experiment, since the safety margins against the HL-LHC most severe accidental scenarios could be established, particularly for MoGr, the baseline bulk material for primary and secondary HL-LHC collimators.

The dynamic behaviour of coatings applied on advanced composites was probed under conditions that exceeded, in terms of energy density, the value expected in HL-LHC, validating the material solution for collimators to be installed in the near future. On top of the effect of temperature, leading to melting in the most loaded region of the coating, spall effects were amplifying the damaged area, which remained however relatively limited in extent.

Online measurements allowed benchmarking in-depth numerical simulations and deriving important properties for the studied materials: for instance, damping ratios were established for all graphitic and diamond-based materials; elastic constants were re-derived, modifying in some cases the quasi-static values available. Mechanical strengths in dynamic conditions were also established for some materials: interestingly, preliminary analyses seem to indicate that strain-rate effects are very limited in the dynamic response of carbonaceous materials.

To complement material data acquired online during the experimental phase, post-irradiation analyses were started once the set-up had reached a manageable level of activation. Computed tomography analyses confirmed the theoretical results, showing cracks originating on the lateral faces of some specimens and propagating towards the core of the sample that had exceeded materials admissible strains in the direction parallel to the basal plane, such as MoGr. Given their nature, these local damages did not undermine the global functionality of the structure.

These observations also allowed deriving the safety factor for MoGr to be used in HL-LHC collimators, since the strain levels at which cracks appeared were a factor of 2 to 3 higher than those expected in the HL-LHC worst accidental scenario. No sign of failure was found neither on CFC nor on graphite given the lower deposited energies that could be achieved. Finally, tomography tests revealed the presence of internal cracks also on TZM and SiC samples, which already underwent macroscopic failure during the tests as a consequence of beam impacts.

Additional non-destructive as well as destructive tests are planned on all the tested specimens, providing further insight on dynamic thermomechanical phenomena and additional valuable information on the investigated materials.

The modularity and reusability of the test-bench will permit performing additional tests in the future, as required.

Acknowledgements This work has received funding from the European Union's Horizon 2020 Research and Innovation programme under Grant Agreement No. 730871. Research supported by CERN HL-LHC project.

References

1. Brüning O et al (2004) LHC design report. CERN Yellow Reports: Monographs, Geneva, Switzerland
2. Apollinari G et al (2017) High-luminosity large hadron collider (HL-LHC) technical design report v.0.1. CERN Yellow Reports: Monographs 4, Geneva, Switzerland
3. Benedikt M et al (2018) Future circular collider study. Volume 3: The Hadron Collider (FCC-hh) Conceptual Design Report, CERN-ACC-2018-0058, Geneva, December 2018. Submitted to Eur. Phys. J. ST
4. Carra F et al (2014) Mechanical engineering and design of novel collimators for HL-LHC. Proc. IPAC 2014, Dresden, Germany
5. Arduini G, Tomas R (2018) H-LHC engineering change request—beam/machine parameters in collision—update. Technical Design Report, Geneva, Switzerland
6. Redaelli S (2016) Beam cleaning and collimation system. In: Proceedings of the joint international accelerator school: beam loss and accelerator protection, Newport Beach, US
7. Carra F et al (2019) Mechanical robustness of HL-LHC collimator designs. Accepted in IPAC19, Melbourne, Australia
8. Efthymiopoulos I et al (2011) HiRadMat: a new irradiation facility for material testing at CERN. In: Proc. IPAC 2011, San Sebastián, Spain
9. Cauchi M et al (2014) High energy beam impact tests on a LHC tertiary collimator at the CERN high-radiation to materials facility. Phys Rev Accel Beams 17:021004
10. Quaranta E et al (2017) Modeling of beam-induced damage of the LHC tertiary collimators. Phys Rev Accel Beams 20:091002
11. Bertarelli A et al (2012) High energy tests of advanced materials for beam intercepting devices at CERN HiRadMat Facility. In: Proceddings of the HB2012, Beijing, China
12. ANSYS Inc (2019) Ansys mechanical user's guide—release 19.2. ANSYS Inc
13. ANSYS Inc (2013) Ansys AUTODYN user's manual—release 15.0 (2013)
14. Gladman B et al (2007) LS-DYNA® keyword user's manual—volume I—Version 971. Livermore Software Technology Corp
15. Bertarelli A et al (2013) Behaviour of advanced materials impacted by high energy particle beams. J Phys Conf Ser 451:1–6
16. Bertarelli A et al (2013) An experiment to test advanced materials impacted by intense proton pulses at CERN HiRadMat facility. Nucl Instrum Method Phys Res B 308:88–99
17. Gobbi G et al (2019) Novel LHC collimator materials: high-energy Hadron beam impact tests and non-destructive post-irradiation examination. J Mech Adv Mater Struct. https://doi.org/10.1080/15376494.2018.1518501
18. Markiewicz T et al (2014) Construction and bench testing of a prototype rotatable collimator for the LHC. In: Proceedings of the IPAC2014, Dresden, Germany
19. Battistoni G et al. (2007) The FLUKA code: description and benchmarking. Hadronic Shower Simulation Workshop, American Institute of Physics, New York
20. Bertarelli A (2016) Beam-induced damage mechanisms and their calculation. CERN Yellow Reports 2:159–227
21. Bertarelli A, Dallocchio A, Kurtyka T (2008) Dynamic response of rapidly heated cylindrical rods: longitudinal and flexural behavior. J Appl Mech 75:1–13

22. Carra F (2017) Thermomechanical response of advanced materials under quasi-instantaneous heating, PhD Thesis, Politecnico di Torino, Italy
23. Tahir N et al (2016) Beam induced hydrodynamic tunneling in the future circular collider components. Phys Rev Accel Beams 19:081002
24. Scapin M et al (2013) Effects induced by LHC high energy beam in copper structures. J Nucl Mat 420:463–472
25. Goodier JN (1937) On the integration of the thermo-elastic equations. Lond Edinb. Dubl. Phil. Mag. J Sci 23:1017–1032
26. Tahir NA et al (2008) The CERN super proton synchrotron as a tool to study high energy density physics. N J Phys 10:1–11
27. Loctite Stycast 2651-40Fr Cat 11, Technical datasheet https://tdsna.henkel.com/NA/UT/HNAUTTDS.nsf/web/77717E3710836804852579C7005C1BB2/$File/STYCAST%202651-40FR%20CAT%2011-EN.pdf
28. Savitzky A, Golay MJ (1964) Smoothing and differentiation of data by simplified least squares procedures. Anal Chem 36:1627–1639
29. Schonbacher H, Tavlet M (1989) Compilation of radiation damage test data, part I. CERN Yellow Reports: Monographs, Geneva, Switzerland
30. Tatsuno Company Limited, http://www.tatsunojapan.com/
31. Brevetti Bizz, http://www.brevettibizz.com/
32. Bertarelli A et al (2015) Innovative MoC—graphite composite for thermal management and thermal shock applications. In: Proceedings of the 31st SEMI-THERM, San Jose, USA
33. Guardia-Valenzuela J et al (2018) Development and properties of high thermal conductivity molybdenum carbide—graphite composites. Carbon 135:72
34. SGL Carbon, https://www.sglcarbon.com/en/markets-solutions/
35. Momentive performance materials, https://www2.momentive.com/
36. CFOAM Ltd, http://www.cfoam.com/
37. Bertarelli A, Carra F, Mariani N, Bizzaro S (2014) Development and testing of novel advanced materials with very high thermal shock resistance. In: Proceedings of the Tungsten, Refractory and Hardmetals Conference, Orlando, USA
38. Scapin M, Fichera C, Carra F, Peroni L (2015) Experimental investigation of the behaviour of tungsten and molybdenum alloys at high strain-rate and temperature. DYMAT2011, Lugano, Switzerland
39. Scapin M, Peroni L, Carra F (2016) Investigation and mechanical modelling of pure molybdenum at high strain-rate and temperature. J Dyn Behav Mater 2:460–475
40. Microcertec, http://www.microcertec.com/index-en.html
41. Furness T et al (2018) Adaptive collimator design for future particle accelerators. In: Proceedings of the IBIC2018, Shanghai, China
42. Peroni L, Scapin M, Carra F, Mariani N (2013) Investigation of dynamic fracture behavior of graphite. In: Basu B (ed) Damage assessment of structures X. Trans Tech Publications Inc, Zurich, pp 103–110
43. Portelli M et al (2019) Numerical and experimental benchmarking of the dynamic response of SiC and TZM specimens in the MultiMat experiment. In preparation
44. Kitzmantel M (2015) Developments and novelties in thermal management by RHP-technology. EuCARD-2 Workshop on Applications of Thermal Management Materials, CERN, Switzerland